

Graphene via large N I: Renormalization

Matthew S. Foster* and Igor L. Aleiner

Department of Physics, Columbia University, New York, NY 10027

(Dated: October 25, 2018)

We analyze the competing effects of moderate to strong Coulomb electron-electron interactions and weak quenched disorder in graphene. Using a one-loop renormalization group calculation controlled within the large- N approximation, we demonstrate that, at successively lower energy (temperature or chemical potential) scales, a type of non-Abelian vector potential disorder always asserts itself as the dominant elastic scattering mechanism for generic short-ranged microscopic defect distributions. Vector potential disorder is tied to both elastic lattice deformations (“ripples”) and topological lattice defects. We identify several well-defined scaling regimes, for which we provide scaling predictions for the electrical conductivity and thermopower, valid when the inelastic lifetime due to interactions exceeds the elastic lifetime due to disorder. Coulomb interaction effects should figure strongly into the physics of suspended graphene films, where $r_s > 1$; we expect vector potential disorder to play an important role in the description of transport in such films.

PACS numbers:

I. INTRODUCTION

The recent experimental realization of graphene,^{1–3} a single atomic monolayer of graphite, has refocused attention upon many fundamental questions regarding electronic transport in low dimensions. Its remarkable bandstructure at zero doping has made graphene a candidate solid state analog for high energy particle phenomena, e.g. that described by the theories of quantum electrodynamics (QED) or chromodynamics (QCD).

Given the relative simplicity of graphene as solid state system, it seemed not unreasonable to hope that a complete understanding of its basic electronic properties would emerge quickly. This expectation has been undermined by several puzzling results in the first graphene experiments.^{1–3} Perhaps most paradoxical is the “quasi-ballistic” nature of its electronic transport: at zero magnetic field, graphene’s conductivity is a linear, particle-hole symmetric function of carrier density that varies little over a temperature range of several orders of magnitude,^{1–3} down to the lowest temperatures so far measured (30 mK).⁴ At exactly zero doping, a condition termed the “Dirac point,” the conductivity assumes a minimum value of order the conductance quantum e^2/h ; this “minimum metallic” conductivity varies only weakly between different samples possessing mobilities spanning an order of magnitude.^{1–4}

One expects that any disorder present must be playing a crucial role in limiting the low-temperature conductivity of undoped graphene. Potentially important sources of disorder in the experiments performed in Refs. 1–5 include remote charged impurities in the SiO₂ substrate,^{6–10} as well as corrugations or “ripples” in the graphene sheet.^{5,11–13} A semiclassical computation within the self-consistent Born approximation (SCBA) at the Dirac point gives a “bare” minimum metallic conductivity independent of the disorder strength, and of order the conductance quantum,^{14–17} in apparent agreement with experiment. Unfortunately, the SCBA is known to

be inconsistent for massless Dirac fermions in 2D.^{18,19} Das Sarma et al.^{8,9} have employed an alternative mean field treatment focused upon charged impurity scattering, and have concluded that the minimum metallic conductivity is in fact not universal, but should exhibit dependence upon the disorder distribution. Near zero doping, Cheianov et al.¹⁰ have further argued that percolation effects become important; these authors used semiclassical percolation theory to derive a scaling form of the conductivity in terms of the transmission coefficient between electron and hole puddles. Other recent analytical^{12,19–22} and numerical^{7,23,24} work has focused upon the localization physics of massless Dirac electrons in the presence of various types of disorder. These and previous^{18,25–29} studies have demonstrated that Dirac electrons may evade Anderson localization for certain fine-tuned disorder distributions, but the relevance of these results to graphene remains unclear.

All of the references discussed above essentially ignore a potentially important aspect of graphene physics, that of electron-electron interactions. Carriers native to the carbon sheet are ineffective at screening the long-ranged Coulomb potential for a system near zero doping. The dimensionless strength of the Coulomb interactions $r_s \sim e^2/\epsilon\hbar v_F$, with v_F the Fermi velocity and ϵ the (effective) dielectric constant, is close to one in the experiments,^{1–5} and should exceed two for suspended films.¹¹ This is not large by the standards of bulk 3D metals. However, it is important to stress that, near the Dirac point, Fermi liquid theory is *not* expected to apply, at least in the absence of disorder. Instead, the situation in graphene is analogous to that in the low-energy domains of QED and QCD in 3 + 1 spacetime dimensions; the smallness of the fine structure constant allows for a consistent perturbative expansion in QED for length scales of order or larger than the Compton wavelength. In the case of QCD, however, the coupling strength is not small at atomic distances, and in fact grows ever larger with increasing length scale. It is not a priori clear

that the Coulomb interparticle interactions in graphene can be treated using perturbation theory in the coupling strength.

For weak Coulomb interactions and disorder, one can use the perturbative renormalization group (RG) to determine whether disorder or interaction effects should become dominant at low temperatures. In this paper, we employ a large- N generalization of the graphene field theory to treat the effects of moderate to strong Coulomb interactions; in physical graphene, $N = 4$ (see Sec. II, below). We study the resulting theory using a one-loop RG calculation perturbative in $1/N$ and in the disorder strength.

The RG has been used many times before to study disorder effects in 2D Dirac fermions,^{19,25,27,28,30} as well as the competition between disorder and interaction effects in such systems.^{31–34} Using a non-interacting model of graphene, Aleiner and Efetov¹⁹ showed that a particular type of disorder, associated with long-wavelength potential fluctuations consistent with, e.g., screened remote charged substrate impurities, dominates the flow to strong coupling in the absence of interactions. Stauber, Guinea, and Vozmediano³³ used the RG to treat both weak disorder and weak Coulomb interactions in graphene; they recovered results previously obtained by Ye and Sachdev.^{31,32} In particular, the weak-coupling RG for graphene demonstrates that a) in the absence of disorder, Coulomb interactions are irrelevant (in the sense of the RG); the non-interacting, clean Dirac description is *stable*, and b) in the presence of generic disorder, the non-interacting, clean Dirac fixed point becomes *unstable*, and the system flows toward strong disorder and interaction coupling. For weak Coulomb interactions, the flow to strong coupling is again dominated by scalar potential disorder, consistent with the formation of local electron and hole “puddles.” This picture would seem to suggest that the asymptotic low-energy physics in disordered graphene should be the same as that in an “ordinary,” diffusive 2D electron gas (but see Refs. 21–24). Multiple crossover regimes are possible depending upon assumptions regarding the microscopic disorder distribution.^{19,20}

Our large- N RG treatment of graphene follows closely a previous calculation of Ye,^{31,32} who employed the same methodology to study strong Coulomb interaction and weak disorder effects in a Dirac system possessing a single Fermi point (generalized to N flavors). Different from Ye, we treat the case of two inequivalent Fermi points (valleys); each valley is generalized to $N/2$ identical flavors. Our calculational framework therefore maintains the important distinction between disorder potentials that scatter particles between inequivalent valleys and those that do not. Further, we correct a calculational mistake made in Ref. 32, the correct determination of which crucially affects our results. (See Sec. III A and Appendix A for details.) Son³⁵ recently revisited the problem of Coulomb interactions at large- N for clean Dirac electrons in graphene; in the limit of vanishing disorder, we recover the findings of Ref. 35.

We now summarize our primary results. We show that, within the large N approximation, disordered graphene resembles QCD more than QED. The theory becomes more strongly coupled at lower temperatures and longer length scales. This eventually leads to a breakdown of our RG calculation, so that we cannot determine the ground state phase within the framework employed here. However, we are able to identify various scaling regimes which may play a role in future experimental observations, particularly in suspended graphene films.¹¹ Our main results are obtained via numerical integration of the RG flow equations, and are as follows: a) The non-interacting, non-disordered Dirac fixed point is unstable upon the incorporation of generic, arbitrarily weak disorder. b) For the case of weak ($r_s \ll 1$) or vanishing Coulomb interactions, the RG flows to strong scalar potential disorder, consistent with the electron-hole puddle picture.^{8–10,19} c) Most importantly, for moderate ($r_s \sim 1$) to strong ($r_s \gg 1$) Coulomb interactions, scalar potential disorder fluctuations are *parametrically* cut off via screening. The system flows to strong interaction and disorder coupling, but now, the runaway flow is dominated by different type of disorder, corresponding to a quenched SU(2) non-Abelian vector potential in the effective Dirac electron theory. This vector potential is implicated in ripples,^{5,11,12,20} as well as the representation of topological lattice defects,³⁶ in the low-energy theory. Finally, we use the RG to predict logarithmic temperature scaling in the dc conductivity within the Drude/Boltzmann transport regime, and we also discuss thermal transport.

The importance of quenched vector potential disorder in the context of graphene has been stressed several times before in the literature.^{5,11,12,20} All of these previous works neglected interparticle interactions, however, and overlooked the important fact that there is no physically plausible way of disordering a graphene sheet that would produce only non-Abelian vector potential disorder in isolation (see Sec. II A, below). Our result establishes that, for moderate to strong Coulomb interactions in the large- N approximation, non-Abelian vector potential disorder emerges *generically* as the dominant source of randomness. Finally, it is intriguing to note that the non-interacting graphene theory subject *only* to non-Abelian vector potential disorder constitutes a very unusual, manifestly particle-hole symmetric quantum disorder model, for which several exact and/or non-perturbative results are known.^{18,20,26} This non-Abelian Dirac disorder model is predicted to *avoid* Anderson localization, possessing instead a perturbatively inaccessible, critical ground state,²⁶ a vanishing disorder-averaged, single-particle density of states,¹⁸ and a non-zero conductivity of order e^2/h , independent of the disorder strength.²⁰

The outline of this paper is as follows. In Sec. II, we write down the low energy field theory for disordered, interacting graphene, and generalize it to the case of large- N in order to treat strong Coulomb interactions. We discuss the microscopic interpretation of the various types of

disorder that appear in the low-energy theory, and we review the quantum disorder universality classes obtained by fine-tuning this distribution. In Sec. III, we perform a one-loop renormalization group calculation upon the model defined in Sec. II. In Sec. IV, we present the results of this calculation, which consist of flow equations for the various parameters defining the graphene field theory. We analyze these equations and attempt to glean information about graphene's phase diagram in an abstract disorder-interaction coupling constant space. Experimental consequences of our results in the form of scaling predictions for the dc conductivity and thermopower are summarized and discussed in Sec. V.

A variety of elaborations and extensions are relegated to the Appendices. Some technical details of the calculation presented in Sec. III are relegated to Appendix A, while a survey of several (unstable) fixed line structures appearing in the flow equations stated in Sec. IV is presented in Appendix B. The scaling predictions enumerated in Sec. V are derived in Appendix C.

II. MODEL AND SETUP

The plan of this section is as follows: In subsection II A, we write down an effective field theory for graphene incorporating both quenched disorder and Coulomb interparticle interactions, and we discuss (1) the role of discrete symmetries and (2) the different universality classes of disordered quantum systems that arise by fine-tuning the details of the impurity or defect distribution. Most of this material is not new, see e.g. Refs. 19,20; the purpose of this section is to provide a context for the results discussed in Sec. IV, and to establish notation. In subsection II B, we construct a large- N generalization of our graphene model, suitable for studying the effects of strong Coulomb interactions.

A. Lattice model and effective field theory

The bandstructure of undoped graphene is well-approximated by the tight-binding Hamiltonian

$$H_0 = -t \sum_{\langle \mathbf{r}\mathbf{r}' \rangle, s} c_{As}^\dagger(\mathbf{r}) c_{Bs}(\mathbf{r}') + \text{H.c.}, \quad (2.1)$$

where $c_{As}^\dagger(\mathbf{r})$ and $c_{Bs}(\mathbf{r}')$ are creation and annihilation operators for electrons on the A and B sublattices of the bipartite honeycomb lattice, respectively. The index $s \in \{\uparrow, \downarrow\}$ denotes spin-1/2 components of the lattice electrons. The hopping amplitude t in Eq. (2.1) is purely real, and the sum on $\langle \mathbf{r}\mathbf{r}' \rangle$ runs over all nearest-neighbor $A - B$ bonds in the graphene sheet. (Further-neighbor hopping may be incorporated as a perturbation). Henceforth we adopt units such that $\hbar = k_B = 1$.

A low-energy effective field theory for undoped graphene obtains by linearizing the bandstructure of

Eq. (2.1) in the vicinity of the two inequivalent K and K' Fermi points (also termed “valleys”), where the particle-hole symmetric energy bands meet. Retaining only low-energy modes, we write

$$c_{\sigma s}(\mathbf{r}) \sim e^{i\mathbf{k}_F \cdot \mathbf{r}} \psi_{\sigma s}^K(\mathbf{r}) + e^{-i\mathbf{k}_F \cdot \mathbf{r}} \psi_{\sigma s}^{K'}(\mathbf{r}), \quad (2.2)$$

where $\pm \mathbf{k}_F$ locates the K and K' points, respectively, and $\sigma \in \{A, B\}$ labels the sublattice species.

We assemble the Dirac spinor

$$\psi(\mathbf{k}) \equiv \begin{bmatrix} \psi_A^K(\mathbf{k}) \\ \psi_B^K(\mathbf{k}) \\ \psi_B^{K'}(\mathbf{k}) \\ -\psi_A^{K'}(\mathbf{k}) \end{bmatrix}. \quad (2.3)$$

(The spin index s has been suppressed in this equation.) In the low-energy theory, we will consider states annihilated by $\psi(\mathbf{k})$ with momentum $k \leq \Lambda \ll k_F$, where Λ is a hard cutoff.

The Dirac spinor defined by Eq. (2.3) is an eight-component object, $\psi \rightarrow \psi_a$, with index $a \in \{1, \dots, 8\}$. The eight components arise from the direct product of indices in the 2-dimensional sublattice $\{A, B\}$, valley $\{K, K'\}$, and spin 1/2 $\{\uparrow, \downarrow\}$ component subspaces. Later, we will generalize ψ_a to $2N$ components in order to perform an expansion in $1/N$. We introduce two commuting sets of Pauli matrices: the matrix $\hat{\sigma}^\alpha$ acts in the sublattice $\{A, B\}$ space of Eq. (2.3), while the matrix $\hat{\kappa}_\beta$ acts in the valley $\{K, K'\}$ space, with $\alpha, \beta \in \{1, 2, 3\}$.³⁷

Below, we write down the continuum field theory for graphene that incorporates the effects of both quenched disorder and Coulomb electron-electron interactions [see Eq. (2.8)]. The clean model in Eq. (2.1) possesses three crucial symmetries that might plausibly survive the incorporation of disorder: particle-hole symmetry (PH), time-reversal invariance (TRI), and spin SU(2) rotational symmetry. In the low-energy theory, the former are encoded in the operator level transformations

$$\psi(\mathbf{r}) \rightarrow -\hat{\sigma}^1 \hat{\kappa}_1 [\psi(\mathbf{r})^\dagger]^\top, \quad (\text{PH}); \quad (2.4)$$

$$\psi(\mathbf{r}) \rightarrow \hat{\sigma}^2 \hat{\kappa}_2 \psi(\mathbf{r}), \quad (\text{TRI}). \quad (2.5)$$

In this equation, \top denotes the ordinary (matrix) transpose. The particle-hole (time-reversal) transformation defined by these equations is unitary (antiunitary). [Schematically writing $H \equiv \psi^\dagger \hat{h} \psi$, c.f. Eq. (2.8), Eq. (2.5) implies that TRI imposes the condition $\hat{\sigma}^2 \hat{\kappa}_2 \hat{h}^* \hat{\sigma}^2 \hat{\kappa}_2 = \hat{h}$ upon the single-particle Hamiltonian \hat{h} .]³⁸ The product of the operations given by Eqs. (2.4) and (2.5) is a so-called “chiral” transformation,^{28,39–42} and was denoted by the symbol “ C_z ” in Ref. 20; in this same reference, the physical TRI [Eq. (2.5)] operation was labeled “ T_0 .”

In addition, it is useful to define two additional transformations, which *do not* correspond to microscopic symmetry operations in the tight-binding honeycomb model of graphene, but nevertheless may play important roles as *emergent* symmetries at a special critical point, or when

additional restrictions are placed upon the disorder distribution:

$$\psi(\mathbf{r}) \rightarrow -\hat{\sigma}^1 \hat{\kappa}_2 [\psi(\mathbf{r})^\dagger]^\top, \quad (\text{PH}^*); \quad (2.6)$$

$$\psi(\mathbf{r}) \rightarrow \hat{\sigma}^2 \psi(\mathbf{r}), \quad (\text{TRI}^*). \quad (2.7)$$

The transformation PH^* is defined to be unitary, while TRI^* is antiunitary. The product of PH^* [Eqs. (2.6)] and the physical TRI operation [Eq. (2.5)] is another type of “chiral” transformation, denoted by the symbol “ C_0 ” in Ref. 20; the TRI^* operation [Eq. (2.7)] was labeled “ T_x ” in this reference.

The effective field theory for undoped graphene is encapsulated by the Hamiltonian

$$H = \int d^2\mathbf{r} \psi^\dagger(\mathbf{r}) \left[-iv_F \hat{\sigma} \cdot \nabla + \hat{\mathcal{V}}(\mathbf{r}) \right] \psi(\mathbf{r}) + \frac{\mathcal{W}}{2} \int d^2\mathbf{r} d^2\mathbf{r}' \frac{\psi^\dagger(\mathbf{r}) \psi^\dagger(\mathbf{r}')}{|\mathbf{r} - \mathbf{r}'|}. \quad (2.8)$$

In this equation, $v_F \sim 3t/2$ is the Fermi velocity, $\hat{\mathcal{V}}(\mathbf{r})$ is a matrix-valued single-particle potential that encodes the structure of the quenched disorder (discussed below), and $\mathcal{W} \sim e^2/\epsilon$ is the microscopic strength of the Coulomb interactions.

We assume that both TRI [Eq. (2.5)] and spin $\text{SU}(2)$ rotational symmetry survive in every static realization of disorder. Our study thus excludes the effects of external magnetic fields or spin-flip impurities, but is appropriate to remote charged impurities, “ripples,”^{5,11–13} non-magnetic interstitial atoms, and topological defects such as dislocations and bound disclination pairs. We will be interested in the properties of a graphene system ensemble-averaged over many realizations of disorder; we presume that such averaging restores invariance under PH transformations [Eq. (2.4)], as well as all honeycomb lattice space group symmetry operations (translations, rotations, reflections). Then the disorder potential $\hat{\mathcal{V}}(\mathbf{r})$ appearing in Eq. (2.8) is conveniently parameterized as

$$\mathcal{V}(\mathbf{r}) \equiv u(\mathbf{r}) \hat{1} + A_{\bar{\alpha}}^{\bar{\beta}}(\mathbf{r}) \hat{\sigma}^{\bar{\alpha}} \hat{\kappa}_{\bar{\beta}} + A_{\bar{\alpha}}^3(\mathbf{r}) \hat{\sigma}^{\bar{\alpha}} \hat{\kappa}_3 + m^{\bar{\beta}}(\mathbf{r}) \hat{\sigma}^3 \hat{\kappa}_{\bar{\beta}} + v(\mathbf{r}) \hat{\sigma}^3 \hat{\kappa}_3. \quad (2.9)$$

In this equation, the barred indices $\bar{\alpha}$ and $\bar{\beta}$ are understood to be summed over the “spatial” Pauli matrix components

$$\bar{\alpha}, \bar{\beta} \in \{1, 2\}. \quad (2.10)$$

Note that Eq. (2.9) implies that potentials $\{A_{\bar{\alpha}}^{\bar{\beta}}\}$ and $\{m^{\bar{\beta}}\}$ scatter between inequivalent Fermi nodes (i.e. couple to the valley space Pauli matrices $\hat{\kappa}_1$ or $\hat{\kappa}_2$); u , $\{A_{\bar{\alpha}}^3\}$, and v do not. Imposing statistical invariance under particle-hole [Eq. (2.4)] and honeycomb lattice space group transformations, and assuming white noise (short-ranged), Gaussian-correlated disorder, we must set the average value of all disorder potentials in Eq. (2.9) to

zero, while we may assign up to five independent parameters $\{g_u, g_A, g_{A3}, g_m, g_v\}$ to characterize their statistical fluctuations:¹⁹

$$\overline{u(\mathbf{r}) u(\mathbf{r}') } = 2\pi g_u v_F^2 \delta^{(2)}(\mathbf{r} - \mathbf{r}'), \quad (2.11a)$$

$$\overline{A_{\bar{\alpha}}^{\bar{\beta}}(\mathbf{r}) A_{\bar{\lambda}}^{\bar{\gamma}}(\mathbf{r}') } = 2\pi g_A v_F^2 \delta_{\bar{\alpha}, \bar{\lambda}} \delta^{\bar{\beta}, \bar{\gamma}} \delta^{(2)}(\mathbf{r} - \mathbf{r}'), \quad (2.11b)$$

$$\overline{A_{\bar{\alpha}}^3(\mathbf{r}) A_{\bar{\lambda}}^3(\mathbf{r}') } = 2\pi g_{A3} v_F^2 \delta_{\bar{\alpha}, \bar{\lambda}} \delta^{(2)}(\mathbf{r} - \mathbf{r}'), \quad (2.11c)$$

$$\overline{m^{\bar{\beta}}(\mathbf{r}) m^{\bar{\gamma}}(\mathbf{r}') } = 2\pi g_m v_F^2 \delta^{\bar{\beta}, \bar{\gamma}} \delta^{(2)}(\mathbf{r} - \mathbf{r}'), \quad (2.11d)$$

$$\overline{v(\mathbf{r}) v(\mathbf{r}') } = 2\pi g_v v_F^2 \delta^{(2)}(\mathbf{r} - \mathbf{r}'). \quad (2.11e)$$

Let us now take a brief excursion from setting up our model to review the physical interpretation of these various disorder types described by Eqs. (2.9) and (2.11); see also Refs. 19,20,36. We will emphasize the connection between the particular types of disorder, the “symmetry” operations defined by Eqs. (2.4)–(2.7), and the different universality classes^{39–41} of disordered quantum systems realized by fine-tuning the disorder distribution in graphene.

1. Scalar potential disorder and the symplectic class AII

Remote charged impurities at or near the substrate surface may provide the dominant scattering mechanism for electrons in the experiments of Refs. 1–5. One expects the potential arising from these impurities to vary relatively slowly on the graphene lattice scale, and therefore to manifest itself primarily through the effective scalar disorder potential $u(\mathbf{r})$ in the low-energy theory [Eqs. (2.8)–(2.11)]. We emphasize that the translation of any lattice-scale disorder potential into the single effective disorder field $u(\mathbf{r})$ is typically impossible, and all disorder types consistent with the underlying symmetry [i.e. time-reversal invariance, Eq. (2.5)] will appear in the low-energy theory. Nevertheless, theoretically we are free to fine-tune the disorder distribution in Eqs. (2.8), (2.9), and (2.11) by setting to zero all disorder parameters except g_u , i.e. only $u(\mathbf{r})$ nonzero. The resulting theory possesses a large $\text{SU}(4)$ symmetry, present in every fixed disorder realization, associated with unitary transformations in (valley) \otimes (spin-1/2) space. In every realization of $u(\mathbf{r})$, this theory is invariant under the alternative “time-reversal” transformation TRI^* , defined by Eq. (2.7). The advent of TRI^* places the non-interacting system [Eqs. (2.8) and (2.9) with $\mathcal{W} = 0$ and only $u(\mathbf{r}) \neq 0$] into the “symplectic” or spin-orbit universality class AII of disordered metals,^{19–25} rather than the orthogonal class AI nominally expected on the basis of spin-1/2 $\text{SU}(2)$ rotational symmetry and “physical” TRI [Eq. (2.5)].⁴³ (We have adopted the nomenclature for quantum disorder classes employed in Refs. 39–41.) Unlike the orthogonal class, the symplectic class is known to possess (in the absence of interactions) a disorder-driven metal-insulator transition in 2D.⁴⁴ The (de-)localization of Dirac electrons subject only to scalar potential disorder has been studied in Refs. 21–24.

2. Vector potential disorder and ripples, topological defects, CI and BDI classes

In the context of graphene, the intravalley Abelian vector potential $\{A_\alpha^3\}$ in Eqs. (2.8) and (2.9) arises in the description of elastic lattice deformations or “ripples.”^{5,11,12,20} Ripples constitute a potentially important source of scattering in the electronic transport of graphene, the presence of which has been directly observed and indirectly inferred in substrate-supported⁵ and suspended¹¹ graphene samples, respectively. Topological lattice defects constitute another class of sample imperfections. In graphene, lattice dislocations can be modeled by point flux insertions of the potential $\{A_\alpha^3\}$ in the low-energy Dirac theory [Eq. (2.8)], while the description of lattice disclinations requires the intervalley components $\{A_\alpha^{\bar{3}}\}$.³⁶ Taken together, $\{A_\alpha^{\bar{3}}\}$ and $\{A_\alpha^3\}$ form a quenched, non-Abelian SU(2) vector potential realized in valley space.

The graphene field theory [Eqs. (2.8) and (2.9)] possessing only quenched SU(2) vector potential disorder, obtained by fine-tuning $u(\mathbf{r}) = m^{\bar{\beta}}(\mathbf{r}) = v(\mathbf{r}) = 0$, is invariant (in every disorder realization) under the alternative “particle-hole” transformation PH*, defined by Eq. (2.6). In the absence of interparticle interactions [$\mathcal{W} = 0$ in Eq. (2.8)], the corresponding disorder-averaged Dirac model with $g_u = g_m = g_v = 0$ in Eq. (2.11) is a critical (i.e. not Anderson localized) conformal field theory (CFT), for which several exact and/or non-perturbative results are known.^{18,26} This CFT realizes a (variant of) the non-Wigner-Dyson universality class CI, typically associated with disordered superconductors.^{18,40,41} Intriguingly, the Dirac theory with only non-Abelian disorder is known to possess a vanishing density of states,¹⁸ and is predicted to exhibit a nonzero conductance, independent of the disorder strength.²⁰ We note, however, that the PH* symmetry transformation given by Eq. (2.6) does not correspond to any local operation in terms of the lattice electrons appearing in the model defined by Eq. (2.1). As a consequence, neither elastic deformations nor topological defects occurring in the lattice-scale description of graphene translate into pure non-Abelian gauge disorder in the low-energy Dirac theory. For example, the field theory description of lattice dislocations and disclinations incorporates the other disorder types $\{u(\mathbf{r}), m^{\bar{\beta}}(\mathbf{r}), v(\mathbf{r})\}$ into the cores of the defects, so that an idealized graphene sheet subject only to topological disorder does *not* realize the CI class CFT.

Potentials $\{A_\alpha^3\}$ and $\{m^{\bar{\gamma}}\}$ preserve both TRI and (physical) particle-hole symmetry (PH) [Eq. (2.4)]. These particle-hole symmetric potentials *can* be mapped to a particular type of “microscopic” disorder consisting of real, nearest-neighbor random hopping on the honeycomb lattice. Such disorder might be realized in principle in a graphene sheet by introducing lattice vacancies, if the only effect of removing a carbon atom is to sever the 3 nearest-neighbor electronic bonds surrounding the va-

cancy (i.e., treating the vacancy in the unitary limit). In the presence of TRI [Eq. (2.5)] and spin SU(2) rotational symmetry, and the absence of interactions ($\bar{w} = 0$) and further-neighbor hopping, such a model with only g_{A3} and g_m non-zero resides in the “chiral” symmetry class BDI,^{27,28,41} and is another example of a critical, delocalized disordered-Dirac model in 2D for which exact and/or non-perturbative results are available.²⁸

3. Staggered on-site potential disorder and class D

Finally, the disorder potential $v(\mathbf{r})$, which couples to a matrix diagonal in both sublattice (σ) and valley (κ) spaces [Eq. (2.9)], may arise in concert with $u(\mathbf{r})$, e.g., in the description of interstitial impurities. The imposition of a *uniform* $v(\mathbf{r}) \equiv v_0$ potential is consistent with the application of an on-site, *A-B* sublattice-staggered chemical potential to the underlying honeycomb lattice model [Eq. (2.1)]. The non-interacting Dirac theory with only staggered potential disorder, Eqs. (2.8) and (2.11) with $\mathcal{W} = 0$ and only $g_v > 0$, realizes the non-Wigner-Dyson class D, and is formally related to the random bond Ising model in 2D.^{25,45–48}

We see that by fine-tuning the details of the disorder distribution within the confines of a graphene sheet that possesses, on average, the full space group symmetry of the honeycomb lattice, several universality classes of (non-interacting) disordered quantum systems may be realized. The realization of these classes is essentially equivalent to imposing various combinations of the discrete symmetries defined by Eqs. (2.4)–(2.7). We emphasize, however, that in the current situation of zero-magnetic field graphene experiments,^{1–5} only the physical time-reversal symmetry [Eq. (2.5)] presumably persists, and the ultimate low-energy, asymptotic physics must be described by the orthogonal Wigner-Dyson class AI.¹⁹ Moreover, the Coulomb interactions are expected to play a strong role, as we will demonstrate in this paper.

We now complete the formal setup of our graphene field theory. We employ the zero-temperature, imaginary time path integral formalism, implementing replicas $\psi \rightarrow \psi_a^i$ in order to average over the disorder. (The index $i \in \{1, 2, \dots, n\}$, with $n \rightarrow 0$ at the end of the calculation). The post-disorder averaged, imaginary time, coherent state path integral is

$$\bar{Z} = \int \mathcal{D}\bar{\psi} \mathcal{D}\psi e^{-\bar{S}}, \quad (2.12)$$

with

$$\begin{aligned}
\bar{S} = & \int d\tau d^2\mathbf{r} \bar{\psi}^i (\partial_\tau - iv_F \hat{\sigma} \cdot \nabla) \psi^i \\
& + \frac{\mathcal{W}}{2} \int d\tau d^2\mathbf{r} d^2\mathbf{r}' \frac{\bar{\psi}^i \psi^i(\mathbf{r}) \bar{\psi}^j \psi^j(\mathbf{r}')}{|\mathbf{r} - \mathbf{r}'|} \\
& - \frac{2\pi g_u v_F^2}{2} \int d\tau d\tau' d^2\mathbf{r} \bar{\psi}^i \psi^i(\tau) \bar{\psi}^j \psi^j(\tau') \\
& - \frac{2\pi \mathcal{G}_\mu^\nu v_F^2}{2} \int d\tau d\tau' d^2\mathbf{r} \bar{\psi}^i \hat{\sigma}^\mu \hat{\kappa}_\nu \psi^i(\tau) \bar{\psi}^j \hat{\sigma}^\mu \hat{\kappa}_\nu \psi^j(\tau'),
\end{aligned} \tag{2.13}$$

where summation is implied over the repeated replica $\{i, j\}$ and disorder vertex $\{\mu, \nu\}$ indices (defined below). The disorder is encoded in the terms on the third and fourth lines of Eq. (2.13), the latter of which involves the disorder “metric”

$$\mathcal{G}_\mu^\nu \rightarrow \begin{bmatrix} g_A & g_A & g_{A3} \\ g_A & g_A & g_{A3} \\ g_m & g_m & g_v \end{bmatrix} \tag{2.14}$$

[c.f. Eqs. (2.9) and (2.11)]. \mathcal{G}_μ^ν couples to the direct product $\hat{\sigma}^\mu \hat{\kappa}_\nu \otimes \hat{\sigma}^\mu \hat{\kappa}_\nu$, with $\mu, \nu \in \{1, 2, 3\}$.

Assuming that frequency carries the (generally scale-dependent) “engineering” dimension

$$[\omega_n] \equiv z, \tag{2.15}$$

measured in inverse-length units, we assign the dimension of the ψ field as

$$[\psi(\tau, \mathbf{r})] \equiv 1. \tag{2.16}$$

Then we find that the Fermi velocity v_F and the Coulomb interaction strength \mathcal{W} share the dimension

$$[v_F] = [\mathcal{W}] = z - 1, \tag{2.17}$$

while the disorder strengths $\{g_u, \mathcal{G}_\mu^\nu\}$ are dimensionless.

B. The theory at $N = \infty$

The field theory given by Eqs. (2.12)–(2.14) was studied by Stauber et al. in Ref. 33 for the case of weak disorder and weak Coulomb interactions. (Their results are discussed in Sec. IV.) In graphene, the effective Coulomb interaction strength is of order unity, calling into question the usefulness of a perturbative expansion in powers of \mathcal{W} [Eq. (2.13)]. In this paper, we employ a large- N generalization in order to treat the case of moderate to strong Coulomb interactions. The expansion parameter $1/N = 1/4$ for physical graphene, which is at least smaller than the bare dimensionless Coulomb interaction strength. Our treatment follows closely that of Ye in Ref. 32, wherein the author considered a large- N generalization of a Dirac theory possessing a single valley.

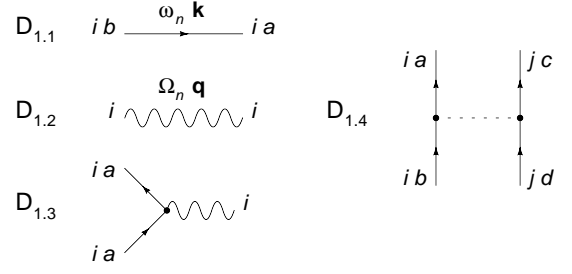


FIG. 1: Diagrammatic elements of the bare Feynman rules. The associated amplitudes are summarized in Table I.

We generalize the Dirac spinor ψ_a^i [Eq. (2.3)] to $2N \gg 1$ components in the index a , with physical graphene corresponding to $N = 4$. [i is the replica index, defined above Eq. (2.12).] Crucially, we will consider only *even* N , retaining the partitioning of N into two inequivalent Fermi point sectors; as above, we will continue to use the Pauli matrices $\hat{\kappa}_m$, $m \in \{1, 2, 3\}$, to address components in this valley space. In other words, we may write $N = 2(2s + 1)$, where we take the spin $s \gg 1$ —formally, this is a large spin expansion. At large N , we consider only the spin-independent, “physical” disorder potentials defined by Eqs. (2.9) and (2.11), acting in the product of sublattice (σ) and valley (κ) spaces.

We begin by decoupling the Coulomb interaction in Eqs. (2.12) and (2.13) with a Hubbard-Stratonovich transformation, using the temporal gauge field a^i (i is again the replica index):

$$\bar{z} \rightarrow \int \mathcal{D}\bar{\psi} \mathcal{D}\psi \mathcal{D}a e^{-\bar{S}}, \tag{2.18}$$

where

$$\begin{aligned}
\bar{S} \rightarrow & \int d\tau d^2\mathbf{r} \bar{\psi}^i \left[\partial_\tau - i\sqrt{\frac{2w}{N}} a^i(\mathbf{r}, 0) - iv_F \hat{\sigma} \cdot \nabla \right] \psi^i \\
& + \frac{1}{2} \int d\tau d^2\mathbf{r} dz \left([\nabla a^i(\mathbf{r}, z)]^2 + [\partial_z a^i(\mathbf{r}, z)]^2 \right) \\
& - \frac{2\pi g_u v_F^2}{2} \int d\tau d\tau' d^2\mathbf{r} \bar{\psi}^i \psi^i(\tau) \bar{\psi}^j \psi^j(\tau') \\
& - \frac{2\pi \mathcal{G}_\mu^\nu v_F^2}{2} \int d\tau d\tau' d^2\mathbf{r} \bar{\psi}^i \hat{\sigma}^\mu \hat{\kappa}_\nu \psi^i(\tau) \bar{\psi}^j \hat{\sigma}^\mu \hat{\kappa}_\nu \psi^j(\tau').
\end{aligned} \tag{2.19}$$

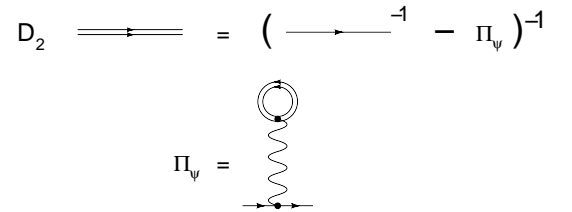


FIG. 2: The fermion propagator at $N = \infty$.

$$D_3 \begin{array}{c} \Omega_n \mathbf{q} \\ i \text{---} \text{wavy} \text{---} i \end{array} = \left(\text{wavy}^{-1} - \Pi_a \right)^{-1}$$

$$\Pi_a = \text{wavy} \text{---} \text{circle} \text{---} \text{wavy}$$

FIG. 3: The gauge (Coulomb) propagator at $N = \infty$.

The temporal gauge field a^i resides in the full 3+1 space-time (τ, \mathbf{r}, z) , while the graphene field theory is confined to the plane $z = 0$. As a result, the coefficient in front of the kinetic term on the second line of Eq. (2.19) cannot be renormalized, as we check explicitly in Sec. III C. In Eq. (2.19), we have replaced $\mathcal{W} \rightarrow w/2\pi N$; we keep w finite and non-zero so as to obtain a well-defined theory in the limit $N \rightarrow \infty$. The bare Feynman rules are stated in Fig. 1 and in Table I. In this paper, we denote each diagram and its corresponding amplitude by the same symbol, $D_{m,n}$, where m is the figure number and n is the particular diagram in question.

The $N \rightarrow \infty$ theory, in the absence of disorder, is completely characterized by the one- and two-particle self-energies depicted in Figs. 2 and 3, respectively. For the special case of massless Dirac fermions studied here, however, particle-hole symmetry prevents the generation of a chemical potential shift, so that the electronic self-energy Π_ψ vanishes at $N = \infty$ (and zero disorder), and the large- N fermion propagator is the same as $D_{1.1}$ (Fig. 1 and Table I).

The gauge field self-energy at $N = \infty$ is depicted in Fig. 3; it is given by the expression

$$\Pi_a(\Omega_n, \mathbf{q}) = (i\sqrt{w/N})^2 \mathcal{D}_0(\Omega_n, \mathbf{q}), \quad (2.20)$$

where the Dirac fermion polarization bubble $\mathcal{D}_0(\Omega_n, \mathbf{q})$ is

$$\mathcal{D}_0(\Omega_n, \mathbf{q}) = \frac{N}{16} \frac{q^2}{\sqrt{\Omega_n^2 + v_F^2 q^2}}. \quad (2.21)$$

Incorporating the self-energy from Eq. (2.20), the propagator for the temporal gauge field at $N = \infty$ and

TABLE I: Factors associated to bare propagators and vertices depicted in Fig. 1.

$D_{1.1}$	=	$\frac{(i\omega_n + v_F \hat{\sigma} \cdot \mathbf{k})_{a,b}}{\omega_n^2 + v_F k^2}$
$D_{1.2}$	=	$\frac{1}{q}$
$D_{1.3}$	=	$i\sqrt{\frac{w}{N}}$
$D_{1.4}$	=	$2\pi g_u v_F^2 \delta_{a,b} \delta_{c,d} + 2\pi \mathcal{G}_\mu^\nu v_F^2 (\hat{\sigma}^\mu \hat{\kappa}_\nu)_{a,b} (\hat{\sigma}^\mu \hat{\kappa}_\nu)_{c,d}$

zero disorder is

$$D_3 = \frac{1}{q} \frac{\sqrt{v_F^2 q^2 + \Omega_n^2}}{\sqrt{v_F^2 q^2 + \Omega_n^2 + \bar{w} v_F |\mathbf{q}|}}, \quad (2.22)$$

where we have introduced the dimensionless Coulomb interaction strength

$$\bar{w} \equiv \frac{w}{16v_F} \quad (2.23)$$

[c.f. Eq. (2.17)]. For the physical case of $N = 4$, the dimensionless parameter \bar{w} is essentially the Coulomb interaction constant r_s :

$$\bar{w} = \frac{\pi}{2} \frac{e^2}{\epsilon v_F}. \quad (2.24)$$

The scalar potential disorder, characterized by the disorder strength g_u [Eqs. (2.9) and (2.11), Fig. 1 and Table I] is parametrically screened by the Dirac sea in the large N limit; the screening affects only the scalar potential disorder, since the other disorder fields in Eq. (2.11) can be understood as arising from charge-neutral defects that produce potentials lacking a monopole (i.e. lowest-order multipole) moment. The diagram D_4 pictured in Fig. 4 gives the complete dressed disorder vertex at $N = \infty$:

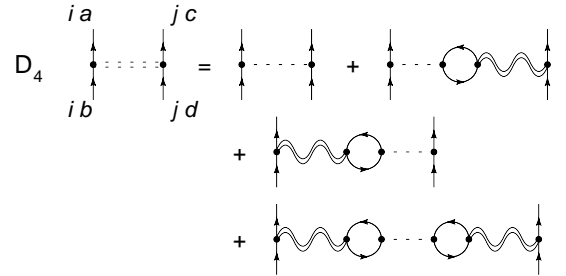
$$D_4 \equiv 2\pi \tilde{g}_u v_F^2 \delta_{a,b} \delta_{c,d} + 2\pi \mathcal{G}_\mu^\nu v_F^2 (\hat{\sigma}^\mu \hat{\kappa}_\nu)_{a,b} (\hat{\sigma}^\mu \hat{\kappa}_\nu)_{c,d}, \quad (2.25)$$

where we have defined the screened scalar potential disorder strength

$$\tilde{g}_u \equiv \frac{g_u}{(1 + \bar{w})^2}. \quad (2.26)$$

In the large- N theory, it is the screened strength \tilde{g}_u , rather than the bare parameter g_u , that appears in physical observables (Sec. V and Appendix C), and therefore characterizes the effective strength of scalar potential fluctuations.

In summary, the Feynman rules for the large- N version of graphene are given by $D_{1.1}$ and $D_{1.3}$ (Fig. 1 and Table I), and by D_3 and D_4 [Figs. 3 and 4, Eqs. (2.22) and (2.25), respectively].

FIG. 4: Screening of the scalar potential disorder g_u due to Coulomb interactions in the $N = \infty$ limit.

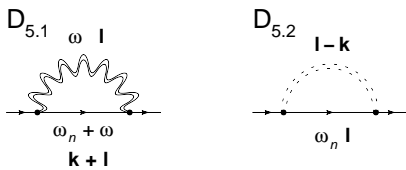


FIG. 5: Corrections to the electronic self-energy at $\mathcal{O}(\frac{1}{N}, \{\tilde{g}_u, \mathcal{G}_\mu^\nu\})$.

III. PERTURBATIVE EXPANSION

In this section, we perform a one-loop renormalization group (RG) calculation within the large- N generalization of graphene defined by Eqs. (2.18) and (2.19). Using the results derived below, we obtain flow equations for the disorder and interaction coupling strengths defined by Eqs. (2.8)–(2.11). These flow equations are stated and analyzed in Sec. IV.

A. Electronic self-energy

We begin with the renormalization of the electronic self-energy due to the disorder and Coulomb interactions (at finite, but large N). The diagrams are depicted in Fig. 5. We consider first the $1/N$ correction due to the interaction, diagram $D_{5.1}$. Expanding in powers of the external frequency ω_n and momentum \mathbf{k} , we find that

$$D_{5.1} \sim -\eta [\bar{w} f_1(\bar{w}) i\omega_n + \bar{w} f_2(\bar{w}) v_F \hat{\sigma} \cdot \mathbf{k}] \ln \Lambda, \quad (3.1)$$

where \bar{w} is the dimensionless Coulomb interaction strength defined by Eq. (2.23), Λ is a hard momentum cutoff, and we have introduced

$$\eta \equiv \frac{8}{\pi N}. \quad (3.2)$$

In Eq. (3.1), the functions $f_1(\bar{w})$ and $f_2(\bar{w})$ denote the following analytic functions of the interaction strength \bar{w}

$$f_1(\bar{w}) = \frac{1}{2} \frac{1}{\sqrt{1-\bar{w}^2}} \left(\frac{1-\sqrt{1-\bar{w}^2}}{1+\sqrt{1-\bar{w}^2}} \right) - \frac{2}{\pi \bar{w}^2} \left[\frac{1-\frac{\bar{w}^2}{2}}{\sqrt{1-\bar{w}^2}} \arcsin(\bar{w}) - \bar{w} \right], \quad (3.3a)$$

$$f_2(\bar{w}) = \frac{1}{2} \frac{1}{1+\sqrt{1-\bar{w}^2}} + \frac{1}{\pi \bar{w}^2} \left[\sqrt{1-\bar{w}^2} \arcsin(\bar{w}) - \bar{w} \right]. \quad (3.3b)$$

It will prove useful to consider the sum

$$f_3(\bar{w}) \equiv f_1(\bar{w}) + f_2(\bar{w}) = \frac{1}{2\bar{w}^2} \left(\frac{2}{\pi} \left[\bar{w} + \frac{\arccos(\bar{w})}{\sqrt{1-\bar{w}^2}} \right] - 1 \right). \quad (3.4)$$

The electronic self-energy contribution detailed in Eqs. (3.1)–(3.4) has been considered several times before in the literature, first by Ye and Sachdev,^{31,32} and soon after by González, Guinea, and Vozmediano.⁴⁹ The interaction self-energy at order $1/N$ was revisited recently by Son.³⁵ Our results agree with those of Refs. 35,49, but disagree with those of Refs. 31,32. We derive Eqs. (3.1)–(3.4) explicitly in Appendix A.

Next, we turn to the disorder diagram $D_{5.2}$. We find

$$D_{5.2} \sim \tilde{\mathcal{G}}_s i\omega_n \ln \Lambda, \quad (3.5)$$

where

$$\begin{aligned} \tilde{\mathcal{G}}_s &\equiv \tilde{g}_u + \sum_{\mu,\nu} \mathcal{G}_\mu^\nu \\ &= \tilde{g}_u + 4g_A + 2g_{A3} + 2g_m + g_v. \end{aligned} \quad (3.6)$$

[\tilde{g}_u is the screened scalar potential disorder strength, defined by Eq. (2.26)].

The bare irreducible two-point vertex function is

$$i\Gamma_{\psi\psi}^{(0)} = i\omega_n - v_F \hat{\sigma} \cdot \mathbf{k} + D_{5.1} + D_{5.2}, \quad (3.7)$$

and the renormalization condition is⁵⁰

$$\frac{d}{d \ln \Lambda} \left(Z_\psi^{\frac{2}{l}} i\Gamma_{\psi\psi}^{(0)} \right) = 0, \quad (3.8)$$

where Z_ψ is the wavefunction renormalization of the ψ field. Using Eqs. (3.1) and (3.5) in Eq. (3.8), and combining the result with the dimensional analysis [Eqs. (2.15)–(2.17)], we obtain the flow equations

$$\frac{d \ln Z_\psi}{dl} = -\eta \bar{w} f_1(\bar{w}) + \tilde{\mathcal{G}}_s, \quad (3.9)$$

$$\frac{d \ln v_F}{dl} = z - 1 - \tilde{\mathcal{G}}_s + \eta \bar{w} f_3(\bar{w}), \quad (3.10)$$

where $l = -\ln \Lambda$ is the log of the RG length scale, and z is the (as yet unspecified) “dynamic critical exponent” [Eq. (2.15)].

Although we are employing a field-theoretic renormalization scheme, Eqs. (3.9) and (3.10) can be equivalently understood in a Wilsonian framework: after an integration of high-momentum modes, one acquires corrections akin to those expressed in Eqs. (3.1) and (3.5). [Consult the action given by Eq. (2.13).] Rescaling momentum $k \rightarrow k/b$, frequency $\omega_n \rightarrow \omega_n/b^z$, and field $\psi \rightarrow Z_\psi^{-1/2} \psi$, one recovers Eqs. (3.9) and (3.10), where $b \sim 1 + dl$.

B. Coulomb vertex

One-loop corrections to the Coulomb vertex $D_{1.3}$ (Fig. 1 and Table I) are depicted in Fig. 6. Most of these diagrams involve a “3-electron ring,” that is, a closed electron loop with three nodes. Such structures are generic to large- N expansions. We note that the graphene (massless Dirac) theory studied here possesses two simplifying features:

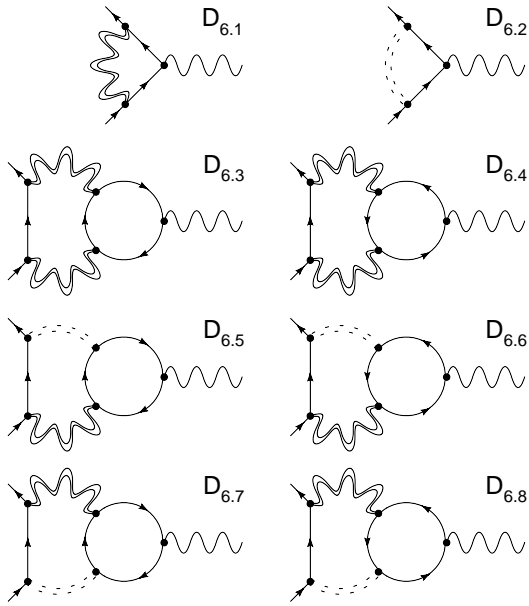


FIG. 6: Coulomb vertex corrections at $O\left(\frac{1}{N}, \{\tilde{\mathcal{G}}_u, \mathcal{G}_\mu^v\}\right)$

- a) The sum of two counter propagating, but otherwise identical, m -electron rings *vanishes* for odd m whenever all m bilinear insertions involve the identity matrix $\hat{1}$; see Fig. 7a. This result is simply a consequence of the odd parity nature of the massless Dirac Green's function $\hat{G}(\mathbf{r})$:

$$\hat{G}(\mathbf{r} - \mathbf{r}') = -\hat{G}(\mathbf{r}' - \mathbf{r}). \quad (3.11)$$

- b) An m -electron ring involving $m - 1$ identity matrix insertions and a single disorder matrix insertion of the form $\hat{M}_{\mu\nu} \equiv \hat{\sigma}^\mu \hat{\kappa}_\nu$ vanishes trivially by the trace over valley (κ) space; see Fig. 7b.

As a result of this simplification, only diagrams $D_{6.1}$ and $D_{6.2}$ contribute. We find that

$$D_{6.1} \sim -\left(i\sqrt{\frac{w}{N}}\right) \eta \bar{w} f_1(\bar{w}) \ln \Lambda, \quad (3.12)$$

and

$$D_{6.2} \sim \left(i\sqrt{\frac{w}{N}}\right) \tilde{\mathcal{G}}_s \ln \Lambda. \quad (3.13)$$

In these equations, $f_1(\bar{w})$ was defined by Eq. (3.3a), η by Eq. (3.2), and $\tilde{\mathcal{G}}_s$ by Eq. (3.6). The evaluation of Eq. (3.12) closely parallels that of the electronic self-energy, the calculation of which is detailed in Appendix A.

The bare vertex function is

$$i\Gamma_{a\psi\psi}^{(0)} \sim \left(i\sqrt{\frac{w}{N}}\right) \left(1 + \ln \Lambda \left[\tilde{\mathcal{G}}_s - \eta \bar{w} f_1(\bar{w})\right]\right). \quad (3.14)$$

Now, we need to know the wavefunction renormalizations for both the Dirac (ψ) and gauge (a) fields to proceed;

the latter requires the evaluation of the gauge field self-energy to one loop. Gauge invariance in fact requires that

$$\frac{d \ln Z_a}{d \ln \Lambda} = 0. \quad (3.15)$$

We will check Eq. (3.15) in Sec. III C, below.

The renormalization condition is therefore

$$\left[\frac{d}{d \ln \Lambda} + \frac{d \ln Z_\psi}{d \ln \Lambda}\right] i\Gamma_{a\psi\psi}^{(0)} = 0, \quad (3.16)$$

which implies the following RG flow equation for the dimensionless Coulomb interaction strength \bar{w} [introduced in Eq. (2.23)]:

$$\frac{d \ln \bar{w}}{dl} = \tilde{\mathcal{G}}_s - \eta \bar{w} f_3(\bar{w}) \quad (3.17)$$

[$l = -\ln \Lambda$ in this equation]. To obtain Eq. (3.17), we have used Eqs. (3.4), (3.9), and (3.10).

C. Gauge field self-energy

The diagrammatic corrections to the gauge field self-energy to be depicted in Figs. 8 and 9. Because of the properties explicated in Fig. 7, the sum of the diagrams in Fig. 9 gives zero.

All of the diagrams in Fig. 8 are formally two-loop, but nevertheless give only contributions to first order in $\ln \Lambda$. In other words, one of the two loops in each of these diagrams is always ultraviolet-finite, and we can obtain their contributions to the renormalization group using the hard momentum cutoff scheme implemented above.

We begin with $D_{8.1}$ and $D_{8.2}$, which give identical contributions. One finds that

$$D_{8.1} + D_{8.2} \sim 2A\bar{w} \frac{v_F q^2}{\sqrt{\Omega_n^2 + v_F^2 q^2}} + 2B\bar{w} \frac{16}{N} v_F J(\Omega_n, \mathbf{q}), \quad (3.18)$$

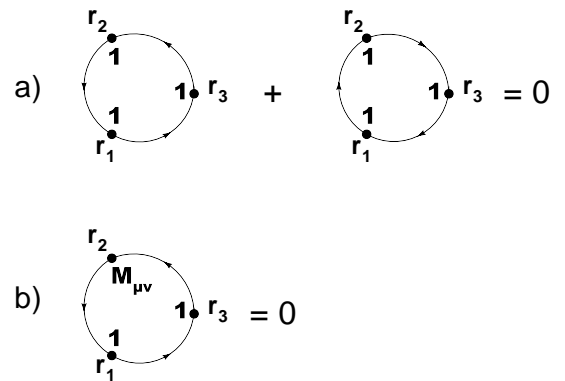


FIG. 7: a) Cancellation between counter-propagating 3-electron rings involving only identity matrix ($\mathbf{1}$) insertions into the trace. b) 3-electron rings involving two identity matrix insertions and one disorder matrix of the form $\hat{M}_{\mu\nu} = \hat{\sigma}^\mu \hat{\kappa}_\nu$ vanish identically.

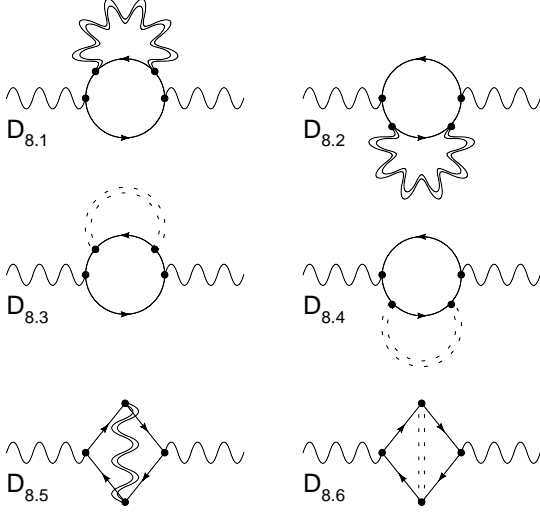


FIG. 8: Corrections to the gauge (Coulomb) field self-energy to $\mathcal{O}(\frac{1}{N}, \{\tilde{g}_u, \mathcal{G}_\mu^\nu\})$.

where we have used Eq. (2.21), and the log-divergent constants A and B follow from Eq. (3.1):

$$A = \frac{1}{2}\eta\bar{w}[f_2(\bar{w}) - f_1(\bar{w})] \ln \Lambda, \quad (3.19a)$$

$$B = -\frac{1}{2}\eta\bar{w}f_3(\bar{w}) \ln \Lambda. \quad (3.19b)$$

In Eq. (3.18), we have defined

$$\begin{aligned} J(\Omega_n, \mathbf{q}) &\equiv \int \frac{d\omega d^2\mathbf{l}}{(2\pi)^3} \frac{\text{Tr} \left[[i(\omega + \Omega_n) + v_F \hat{\sigma} \cdot (\mathbf{l} + \mathbf{q})] \right.}{[\omega^2 + v_F^2 \mathbf{l}^2]^2 [(\omega + \Omega_n)^2 + v_F^2 (\mathbf{l} + \mathbf{q})^2]} \\ &= \frac{N}{16} \frac{q^2 \Omega_n^2}{(v_F^2 q^2 + \Omega_n^2)^{\frac{3}{2}}}. \end{aligned} \quad (3.20)$$

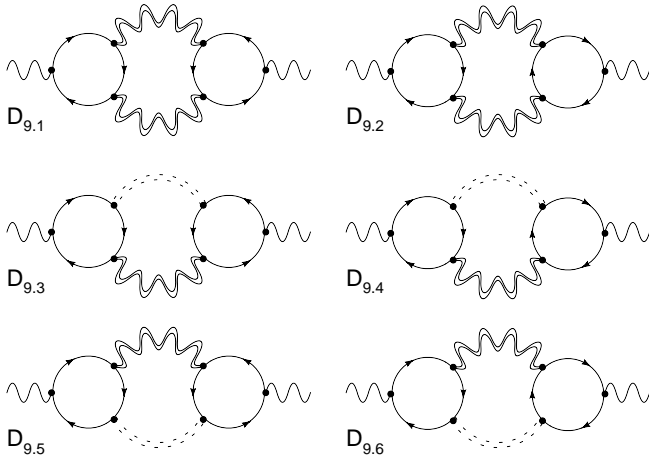


FIG. 9: Corrections to the gauge (Coulomb) field self-energy to $\mathcal{O}(\frac{1}{N}, \{\tilde{g}_u, \mathcal{G}_\mu^\nu\})$.

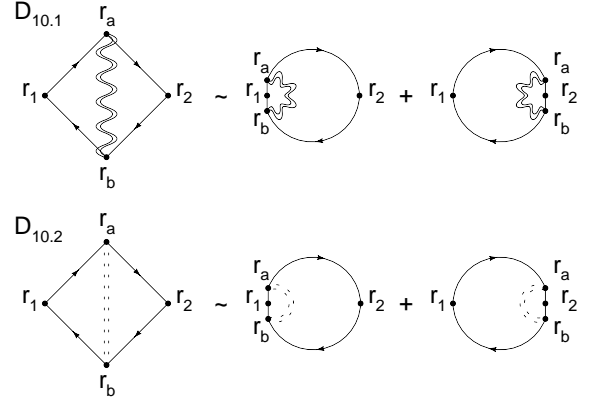


FIG. 10: Evaluation of “two-loop” diagrams $D_{8.5}$ and $D_{8.6}$ in Fig. 8. These graphs can be expressed in terms of products of an ultraviolet-convergent polarization bubble and an ultraviolet-divergent vertex correction (see Fig. 6).

Next, we evaluate

$$\begin{aligned} D_{8.3} + D_{8.4} &= 2A'\bar{w} \frac{v_F q^2}{\sqrt{\Omega_n^2 + v_F^2 q^2}} + 2B'\bar{w} \frac{v_F q^2 \Omega_n^2}{(\Omega_n^2 + v_F^2 q^2)^{\frac{3}{2}}}. \end{aligned} \quad (3.21)$$

In Eq. (3.21), the log-divergent constants A' and B' follow from Eq. (3.5):

$$A' = B' = \frac{1}{2}\tilde{\mathcal{G}}_s \ln \Lambda. \quad (3.22)$$

Diagrams $D_{8.5}$ and $D_{8.6}$ can be evaluated by simply multiplying the divergent vertex correction [Eqs. (3.12) and (3.13)] (evaluated at the left *and* right sides of the two-loop graphs, as shown in Fig. 10) by a factor of the non-divergent polarization bubble, given by the $N = \infty$ photon self-energy [Eq. (2.20)]. We obtain

$$D_{8.5} \sim 2\eta\bar{w}^2 f_1(\bar{w}) \ln \Lambda \frac{v_F q^2}{\sqrt{\Omega_n^2 + v_F^2 q^2}}, \quad (3.23a)$$

$$D_{8.6} \sim -2\bar{w}\tilde{\mathcal{G}}_s \ln \Lambda \frac{v_F q^2}{\sqrt{\Omega_n^2 + v_F^2 q^2}}. \quad (3.23b)$$

Summing the results of Eqs. (3.18), (3.21), and (3.23) with the inverse $N = \infty$ gauge propagator [Eq. (2.22)], and using Eqs. (3.19) and (3.22), we obtain the bare ver-

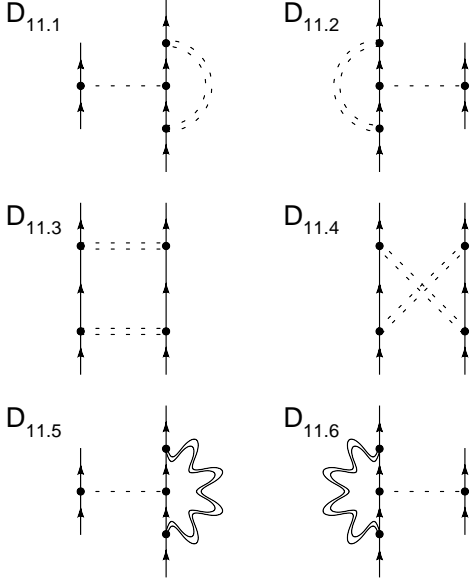


FIG. 11: Renormalization of the disorder strength at $\mathcal{O}(\frac{g}{N}, g^2)$, where $g \in \{\tilde{g}_u, \mathcal{G}_\mu^\nu\}$.

tex function

$$\begin{aligned}
i\Gamma_{aa}^{(0)} = & -|\mathbf{q}| - \bar{w} \frac{v_F q^2}{\sqrt{\Omega_n^2 + v_F^2 q^2}} \\
& + \frac{v_F q^2}{\sqrt{\Omega_n^2 + v_F^2 q^2}} \left[\eta \bar{w}^2 f_3(\bar{w}) - \bar{w} \tilde{\mathcal{G}}_s \right] \ln \Lambda \\
& + \frac{v_F q^2 \Omega_n^2}{(\Omega_n^2 + v_F^2 q^2)^{\frac{3}{2}}} \left[-\eta \bar{w}^2 f_3(\bar{w}) + \bar{w} \tilde{\mathcal{G}}_s \right] \ln \Lambda.
\end{aligned} \tag{3.24}$$

Since there is no correction proportional to $|\mathbf{q}|$, we see immediately that

$$\frac{d \ln Z_a}{d \ln \Lambda} = 0, \tag{3.25}$$

as assumed above in Eq. (3.15). The renormalization condition is then

$$\frac{d}{d \ln \Lambda} i\Gamma_{aa}^{(0)} = 0. \tag{3.26}$$

Eq. (3.26) recovers the previously-derived results, Eqs. (3.10) and (3.17).

D. Disorder strength renormalization

Finally, we compute the renormalization of the disorder strength, using the diagrams pictured in Fig. 11–13. These diagrams correct the *bare* disorder vertex $D_{1,4}$, pictured in Fig. 1, with the tree-level amplitude given in Table I.

Diagrams $D_{11.1}$ – $D_{11.4}$ describe the autorenormalization of the disorder at one loop. One finds¹⁹

$$\begin{aligned}
& D_{11.1} + D_{11.2} + D_{11.3} + D_{11.4} \\
& = 2\pi v_F^2 (\hat{1} \otimes \hat{1}) \left[2g_u \tilde{\mathcal{G}}_s + 8g_m g_A + 4g_v g_{A3} \right] \ln \Lambda \\
& + 2\pi v_F^2 (\hat{\sigma}^{\bar{\alpha}} \hat{\kappa}_{\bar{\beta}} \otimes \hat{\sigma}^{\bar{\alpha}} \hat{\kappa}_{\bar{\beta}}) \left[\frac{8g_{A3} g_A}{+ 2g_m (\tilde{g}_u + g_v)} \right] \ln \Lambda \\
& + 2\pi v_F^2 (\hat{\sigma}^{\bar{\alpha}} \hat{\kappa}_3 \otimes \hat{\sigma}^{\bar{\alpha}} \hat{\kappa}_3) \left[2g_m^2 + 8g_A^2 + 2\tilde{g}_u g_v \right] \ln \Lambda \\
& + 2\pi v_F^2 (\hat{\sigma}^3 \hat{\kappa}_{\bar{\beta}} \otimes \hat{\sigma}^3 \hat{\kappa}_{\bar{\beta}}) \left[\frac{2g_m (g_v - \tilde{g}_u)}{+ 4g_A (\tilde{g}_u + g_v)} \right] \ln \Lambda \\
& + 2\pi v_F^2 (\hat{\sigma}^3 \hat{\kappa}_3 \otimes \hat{\sigma}^3 \hat{\kappa}_3) \left[\frac{2g_v (2g_m - \tilde{g}_u - g_v)}{+ 4g_{A3} (\tilde{g}_u + g_v)} \right. \\
& \quad \left. + 8g_A (g_m - g_v) \right] \ln \Lambda,
\end{aligned} \tag{3.27}$$

where we have re-introduced the following notation: barred Greek indices run over the “spatial” Pauli matrix components

$$\bar{\alpha}, \bar{\beta} \in \{1, 2\}, \tag{3.28}$$

to be distinguished from unbarred Greek indices which run over all three Pauli matrix components, e.g.

$$\alpha, \beta \in \{1, 2, 3\}. \tag{3.29}$$

Diagrams $D_{11.5}$ and $D_{11.6}$ give identical contributions, involving the dressing of the disorder vertex by the Coulomb interactions at $\mathcal{O}(1/N)$. Their evaluation proceeds similarly to that of the electronic self-energy (detailed in Appendix A). We obtain

$$\begin{aligned}
& D_{11.5} + D_{11.6} \\
& = 2\pi g_u v_F^2 (\hat{1} \otimes \hat{1}) [-2\eta \bar{w} f_1(\bar{w})] \ln \Lambda \\
& + 2\pi g_A v_F^2 (\hat{\sigma}^{\bar{\alpha}} \hat{\kappa}_{\bar{\beta}} \otimes \hat{\sigma}^{\bar{\alpha}} \hat{\kappa}_{\bar{\beta}}) [2\eta \bar{w} f_2(\bar{w})] \ln \Lambda \\
& + 2\pi g_{A3} v_F^2 (\hat{\sigma}^{\bar{\alpha}} \hat{\kappa}_3 \otimes \hat{\sigma}^{\bar{\alpha}} \hat{\kappa}_3) [2\eta \bar{w} f_2(\bar{w})] \ln \Lambda \\
& + 2\pi g_m v_F^2 (\hat{\sigma}^3 \hat{\kappa}_{\bar{\beta}} \otimes \hat{\sigma}^3 \hat{\kappa}_{\bar{\beta}}) \left[\frac{2\eta \bar{w} f_2(\bar{w})}{+ 2\eta \bar{w} f_3(\bar{w})} \right] \ln \Lambda \\
& + 2\pi g_v v_F^2 (\hat{\sigma}^3 \hat{\kappa}_3 \otimes \hat{\sigma}^3 \hat{\kappa}_3) \left[\frac{2\eta \bar{w} f_2(\bar{w})}{+ 2\eta \bar{w} f_3(\bar{w})} \right] \ln \Lambda.
\end{aligned} \tag{3.30}$$

The functions $f_1(\bar{w})$ – $f_3(\bar{w})$ were defined by Eqs. (3.3) and (3.4).

The remaining diagrams pictured in Figs. 12 and 13 involve 3-electron loops. We consider first the ring dia-

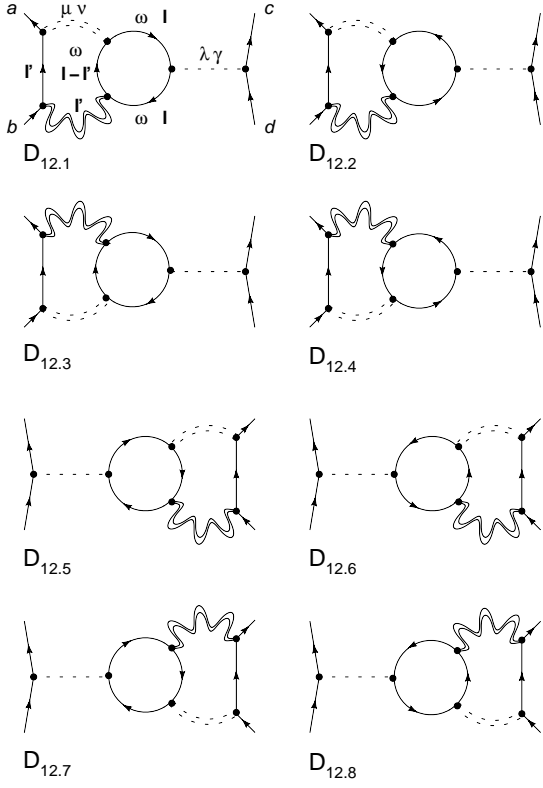


FIG. 12: Renormalization of the disorder strength at $\mathcal{O}(\frac{g}{N}, g^2)$, where $g \in \{\bar{g}_u, \mathcal{G}_\mu^\nu\}$.

grams in Fig. 12, beginning with $D_{12.1}$:

$$\begin{aligned}
 D_{12.1} = & 2\pi \mathcal{G}_\mu^\nu v_F^2 2\pi \mathcal{G}_\lambda^\gamma v_F^2 (\hat{\sigma}^\lambda \hat{\kappa}_\gamma)_{c,d} \left(i\sqrt{\frac{w}{N}} \right)^2 \frac{-1}{1+\bar{w}} \\
 & \times \int \frac{d\omega d^2\mathbf{l} d^2\mathbf{l}'}{(2\pi)^5} \frac{[\hat{\sigma}^\mu \hat{\kappa}_\nu v_F \hat{\sigma} \cdot \mathbf{l}']_{a,b}}{v_F^2 \mathbf{l}'^2} \frac{1}{|\mathbf{l}'|} \\
 & \text{Tr} \begin{pmatrix} \hat{\sigma}^\mu \hat{\kappa}_\nu [i\omega + v_F \hat{\sigma} \cdot (\mathbf{1} - \mathbf{l}')] \\ \times [i\omega + v_F \hat{\sigma} \cdot \mathbf{l}] \hat{\sigma}^\lambda \hat{\kappa}_\gamma \\ \times [i\omega + v_F \hat{\sigma} \cdot \mathbf{l}] \end{pmatrix} \\
 & \times \frac{1}{[\omega^2 + v_F^2 \mathbf{l}'^2]^2 [\omega^2 + v_F^2 (\mathbf{1} - \mathbf{l}')^2]}. \quad (3.31)
 \end{aligned}$$

Simplifying, we obtain

$$\begin{aligned}
 D_{12.1} = & (2\pi)^2 \mathcal{G}_\mu^\nu \mathcal{G}_\lambda^\gamma v_F^2 (\hat{\sigma}^\mu \hat{\kappa}_\nu \hat{\sigma}^{\bar{\alpha}})_{a,b} (\hat{\sigma}^\lambda \hat{\kappa}_\nu)_{c,d} \frac{2^5 i\bar{w}}{1+\bar{w}} \\
 & \times \left[\epsilon_{\mu\lambda\bar{\beta}} K_1^{\bar{\alpha},\bar{\beta}} + \delta_{\bar{\beta},\bar{\xi}} \epsilon_{\mu\lambda\bar{\eta}} K_2^{\bar{\alpha},\bar{\beta},\bar{\eta},\bar{\xi}} \right. \\
 & \left. - (\delta_{\mu,\bar{\xi}} \epsilon_{\lambda\bar{\eta}\bar{\beta}} + \delta_{\lambda,\bar{\xi}} \epsilon_{\mu\bar{\eta}\bar{\beta}}) K_2^{\bar{\alpha},\bar{\beta},\bar{\eta},\bar{\xi}} \right], \quad (3.32)
 \end{aligned}$$

where

$$\begin{aligned}
 K_1^{\bar{\alpha},\bar{\beta}} & \equiv \int \frac{d\omega d^2\mathbf{l} d^2\mathbf{l}'}{(2\pi)^5} \frac{l'^{\bar{\alpha}} (1 - \mathbf{l}')^{\bar{\beta}} \omega^2}{|\mathbf{l}'|^3 [\omega^2 + \mathbf{l}'^2]^2 [\omega^2 + (\mathbf{1} - \mathbf{l}')^2]}, \\
 & \sim -\frac{12 \ln \Lambda}{2^{10} 2\pi} \delta^{\bar{\alpha},\bar{\beta}}, \quad (3.33)
 \end{aligned}$$

and

$$\begin{aligned}
 K_2^{\bar{\alpha},\bar{\beta},\bar{\eta},\bar{\xi}} & \equiv \int \frac{d\omega d^2\mathbf{l} d^2\mathbf{l}'}{(2\pi)^5} \frac{l'^{\bar{\alpha}} (1 - \mathbf{l}')^{\bar{\beta}} l^{\bar{\eta}} l^{\bar{\xi}}}{|\mathbf{l}'|^3 [\omega^2 + \mathbf{l}'^2]^2 [\omega^2 + (\mathbf{1} - \mathbf{l}')^2]}, \\
 & \sim \frac{1}{2^{10}} \frac{\ln \Lambda}{2\pi} \left[3(\delta^{\bar{\alpha},\bar{\eta}} \delta^{\bar{\beta},\bar{\xi}} + \delta^{\bar{\alpha},\bar{\xi}} \delta^{\bar{\beta},\bar{\eta}}) \right. \\
 & \left. - 13(\delta^{\bar{\alpha},\bar{\beta}} \delta^{\bar{\eta},\bar{\xi}}) \right]. \quad (3.34)
 \end{aligned}$$

Eqs. (3.33) and (3.34) may be obtained by a) performing the ultraviolet-convergent 3-electron loop momentum integral over \mathbf{l} via Feynman parameters, b) evaluating the frequency integration over the real line, and c) completing the final ultraviolet-divergent momentum integral over \mathbf{l}' .

Combining Eqs. (3.32)–(3.34), and carefully summing barred (unbarred) indices over $\{1, 2\}$ ($\{1, 2, 3\}$), we finally obtain

$$\begin{aligned}
 D_{12.1} \sim & \frac{v_F^2 \bar{w}}{1+\bar{w}} \frac{\ln \Lambda}{2} \left(2\pi (\hat{\sigma}^3 \hat{\kappa}_{\bar{\beta}} \otimes \hat{\sigma}^3 \hat{\kappa}_{\bar{\beta}}) [-4g_m g_A] \right. \\
 & \left. + 2\pi (\hat{\sigma}^3 \hat{\kappa}_3 \otimes \hat{\sigma}^3 \hat{\kappa}_3) [-4g_v g_{A3}] \right). \quad (3.35)
 \end{aligned}$$

The remaining diagrams in Fig. 12 give identical contributions. Next, we consider the diagrams shown in Fig. 13. Each of the diagrams $D_{13.1}$ – $D_{13.4}$ represents an autorenormalization of the bare scalar potential disorder parameter g_u , mediated by the Coulomb interaction \bar{w} . Due to the 3-ring cancellation property encapsulated by Fig. 7, the sum of these diagrams gives (exactly) zero.

The bare vertex function is

$$\begin{aligned}
 i\Gamma_D^{(0)} = & 2\pi g_u v_F^2 (\hat{\mathbf{1}} \otimes \hat{\mathbf{1}}) \\
 & + 2\pi \mathcal{G}_\mu^\nu v_F^2 (\hat{\sigma}^\mu \hat{\kappa}_\nu) \otimes (\hat{\sigma}^\mu \hat{\kappa}_\nu) \\
 & + D_{11} + D_{12}, \quad (3.36)
 \end{aligned}$$

where D_m , $m \in \{11, 12\}$, denotes the sum of all diagrams in Fig. m .

The renormalization condition is

$$\left[\frac{d}{d \ln \Lambda} + 2 \frac{d \ln Z_\psi}{d \ln \Lambda} \right] i\Gamma_D^{(0)} = 0, \quad (3.37)$$

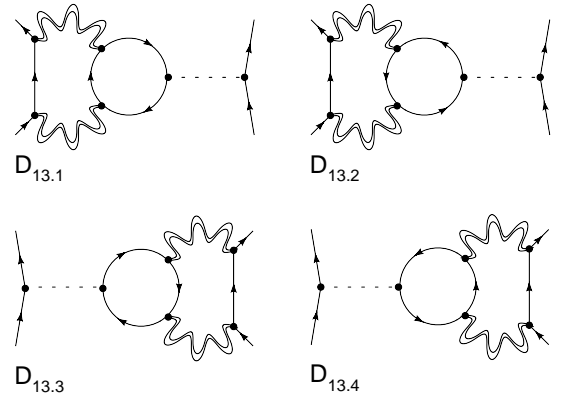


FIG. 13: Renormalization of the disorder strength at $\mathcal{O}(\frac{g}{N}, g^2)$, where $g \in \{\bar{g}_u, \mathcal{G}_\mu^\nu\}$.

which leads to the renormalization group flow equations

$$\frac{dg_u}{dl} = 2g_u \left[\tilde{\mathcal{G}}_s - \eta \bar{w} f_3(\bar{w}) \right] + 8g_m g_A + 4g_v g_{A3}, \quad (3.38a)$$

$$\frac{dg_A}{dl} = 8g_A g_{A3} + 2g_m(\tilde{g}_u + g_v), \quad (3.38b)$$

$$\frac{dg_{A3}}{dl} = 2g_m^2 + 8g_A^2 + 2\tilde{g}_u g_v, \quad (3.38c)$$

$$\begin{aligned} \frac{dg_m}{dl} = & 2g_m(g_v - \tilde{g}_u) + 4g_A(\tilde{g}_u + g_v) + 2g_m \eta \bar{w} f_3(\bar{w}) \\ & - \frac{16\bar{w}}{1+\bar{w}} g_m g_A, \end{aligned} \quad (3.38d)$$

$$\begin{aligned} \frac{dg_v}{dl} = & 2g_v(2g_m - \tilde{g}_u - g_v) + 4g_{A3}(\tilde{g}_u + g_v) \\ & + 8g_A(g_m - g_v) + 2g_v \eta \bar{w} f_3(\bar{w}) - \frac{16\bar{w}}{1+\bar{w}} g_v g_{A3}, \end{aligned} \quad (3.38e)$$

where we have used Eqs. (3.4), Eqs. (3.9), and (3.17). $[\tilde{\mathcal{G}}_s$ was defined by Eq. (3.6).]

IV. ANALYSIS OF THE RENORMALIZATION GROUP FLOWS

In this section, we use the results of our one-loop renormalization group (RG) study, detailed in Sec. III, to attempt to understand the topology of graphene's phase diagram in disorder–interaction coupling strength space. Our primary goal is to determine *what kind* of low-energy theory one should use to understand the macroscopic electronic properties of a graphene sheet, using the RG as our guide. If the RG reveals a theoretically tractable (e.g., perturbatively accessible) phase or critical point, then we can use that framework to make predictions that can be tested against experiment. As we will see, the situation appears to be more complex (at least to lowest order in $1/N$), and the ultimate low-energy physics (at zero temperature) likely requires a description very different from the weakly-perturbed, massless Dirac electron picture used as our starting point here.

Nevertheless, the RG does allow us to identify several possible scaling regimes; our most interesting result concerns the apparent robustness of one such scaling regime, at least as viewed from the vantage point of the weakly-disordered Dirac electron theory. This (crossover) regime turns out to be dominated by the non-Abelian vector potential disorder, characterized by the parameters g_A and g_{A3} [Eqs. (2.9) and (2.11)] which appear, e.g., in the description of elastic lattice deformations (“ripples”),^{5,11–13} as well as topological defects in the graphene lattice (Sec. II A 2 and Refs. 20,36). This principal result is demonstrated via numerical integration of the RG flows, and is discussed in subsection IV E, below. Potential experimental manifestations of our results are discussed in Sec. V.

A. One-loop flow equations

Using renormalized perturbation theory, we obtained in the previous section the one-loop flow equations for the coupling constants of the large- N graphene field theory defined by Eq. (2.19). Six coupling strengths define that model: the Fermi velocity v_F , the dimensionless Coulomb interaction strength \bar{w} [Eqs. (2.23) and (2.24)], the screened scalar potential disorder strength \tilde{g}_u [Eq. (2.26)], as well as g_A , g_{A3} , g_m , and g_v [Eqs. (2.8)–(2.11)]. The latter four disorder parameters were encoded in the disorder metric \mathcal{G}_μ^ν , defined by Eq. (2.14). From Eqs. (3.10), (3.17), and (3.38) obtained in Sec. III, the flow equations to the lowest nontrivial order in the small parameters $1/N$ and $\{\tilde{g}_u, \mathcal{G}_\mu^\nu\}$ are given by

$$\frac{d \ln v_F}{dl} = z - 1 - \tilde{\mathcal{G}}_s + \eta \bar{w} f_3(\bar{w}), \quad (4.1a)$$

$$\frac{d \ln \bar{w}}{dl} = \tilde{\mathcal{G}}_s - \eta \bar{w} f_3(\bar{w}), \quad (4.1b)$$

$$\frac{d \tilde{g}_u}{dl} = \frac{2\tilde{g}_u}{1+\bar{w}} \left[\tilde{\mathcal{G}}_s - \eta \bar{w} f_3(\bar{w}) \right] + \frac{8g_m g_A + 4g_v g_{A3}}{(1+\bar{w})^2}, \quad (4.1c)$$

$$\frac{dg_A}{dl} = 8g_A g_{A3} + 2g_m(\tilde{g}_u + g_v), \quad (4.1d)$$

$$\frac{dg_{A3}}{dl} = 2g_m^2 + 8g_A^2 + 2\tilde{g}_u g_v, \quad (4.1e)$$

$$\begin{aligned} \frac{dg_m}{dl} = & 2g_m(g_v - \tilde{g}_u) + 4g_A(\tilde{g}_u + g_v) + 2g_m \eta \bar{w} f_3(\bar{w}) \\ & - \frac{16\bar{w} g_m g_A}{1+\bar{w}}, \end{aligned} \quad (4.1f)$$

$$\begin{aligned} \frac{dg_v}{dl} = & 2g_v(2g_m - \tilde{g}_u - g_v) + 4g_{A3}(\tilde{g}_u + g_v) \\ & + 8g_A(g_m - g_v) + 2g_v \eta \bar{w} f_3(\bar{w}) - \frac{16\bar{w} g_v g_{A3}}{1+\bar{w}}. \end{aligned} \quad (4.1g)$$

In these equations,

$$\tilde{\mathcal{G}}_s \equiv \tilde{g}_u + 4g_A + 2g_{A3} + 2g_m + g_v, \quad (4.2)$$

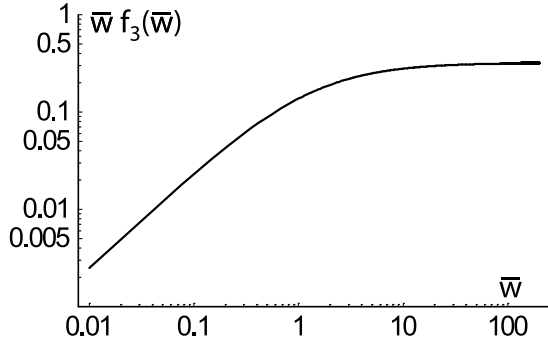
and

$$\eta \equiv \frac{8}{\pi N}. \quad (4.3)$$

In Eq. (4.1a), $z = z(l)$ is the (as yet unspecified) dynamic critical exponent. The function $f_3(\bar{w})$ appearing in Eq. (4.1) was defined by Eq. (3.4), repeated below for convenience:

$$f_3(\bar{w}) = \frac{1}{2\bar{w}^2} \left[\frac{2}{\pi} \left[\bar{w} + \frac{\arccos(\bar{w})}{\sqrt{1-\bar{w}^2}} \right] - 1 \right], \quad (4.4)$$

valid for $\bar{w} \leq 1$. The analytical continuation of $f_3(\bar{w})$ for

FIG. 14: Plot of $\bar{w} f_3(\bar{w})$.

$\bar{w} \geq 1$ is given by

$$f_3(\bar{w}) = \frac{1}{2\bar{w}^2} \left(-1 + \frac{2\bar{w}}{\pi} + \frac{2}{\pi\sqrt{\bar{w}^2 - 1}} \ln(\bar{w} + \sqrt{\bar{w}^2 - 1}) \right). \quad (4.5)$$

In the small and large \bar{w} limits, $f_3(\bar{w})$ has the behaviors

$$\begin{aligned} f_3(\bar{w}) &\sim \frac{1}{4} - \frac{2\bar{w}}{3\pi} + \frac{3\bar{w}^2}{16} + \dots & 0 \leq \bar{w} \ll 1, \\ &\sim \frac{1}{\pi\bar{w}} + \mathcal{O}\left(\frac{1}{\bar{w}^2}\right), & \bar{w} \gg 1. \end{aligned} \quad (4.6)$$

The function $\bar{w} f_3(\bar{w})$ is plotted in Fig. 14.

Eq. (4.1c) follows from the definition of the screened scalar potential disorder strength \tilde{g}_u [Eq. (2.26)], and the flow equation (3.38a) for the bare scalar potential strength. We emphasize that it is \tilde{g}_u that appears in physical quantities in the large- N theory, as demonstrated in Sec. V; the renormalization group must therefore be formulated in terms of \tilde{g}_u , the effective scalar potential strength.

B. Termination of the RG flow for finite temperatures and chemical potential

The derived RG equations (4.1) are limited by the regime of the weak disorder strength and usually become non-usable when $l \rightarrow \infty$. There are, however, physical situations when those equations are adequate to determine the transport properties of the system. Those are regimes of either sufficiently large doping (characterized by the chemical potential μ), or of sufficiently high temperature T . At such an energy scale, the logarithmic renormalizations must be stopped, and kinetic coefficients computed, as in Sec. V.

To use Eqs. (4.1) we have to relate the scale l_* at which the RG is stopped to the energy scale

$$\varepsilon_* \simeq \max(|\mu|, T). \quad (4.7)$$

To achieve this goal, we write a scaling equation

$$\frac{d \ln \varepsilon_*}{dl_*} = -z(l_*), \quad (4.8)$$

and find the scale-dependent dynamic critical exponent by setting Eq. (4.1a) equal to zero.^{34,51} It gives us an implicit function $l_*(\varepsilon_*)$

$$\begin{aligned} \ln \frac{\varepsilon_* a}{v_F^{(a)}} &= - \int_0^{l_*} dl z(l); \\ z(l) &= 1 + \tilde{\mathcal{G}}_s(l) - \eta \bar{w}(l) f_3[\bar{w}(l)], \end{aligned} \quad (4.9)$$

where $v_F^{(a)}$ is the Fermi velocity defined on the spatial scale of the order of lattice constant a .

C. Restricted flow equations: SU(2) valley space rotation symmetry restored

A useful subset of the RG flow provided by Eq. (4.1) is to consider the system with SU(2) valley (κ) space rotational symmetry restored *on average*. Such a restriction constrains

$$\begin{aligned} g_A &= g_{A3}, \\ g_m &= g_v. \end{aligned} \quad (4.10)$$

[See Eqs. (2.9) and (2.11).] Imposing Eq. (4.10), the RG equations reduce to

$$\frac{d \ln v_F}{dl} = z - 1 - (\tilde{g}_u + 6g_A + 3g_m) + \eta \bar{w} f_3(\bar{w}) \quad (4.11a)$$

$$\frac{d \ln \bar{w}}{dl} = (\tilde{g}_u + 6g_A + 3g_m) - \eta \bar{w} f_3(\bar{w}), \quad (4.11b)$$

$$\begin{aligned} \frac{d \tilde{g}_u}{dl} &= \frac{2\tilde{g}_u}{1 + \bar{w}} [\tilde{g}_u + 6g_A + 3g_m - \eta \bar{w} f_3(\bar{w})] \\ &\quad + \frac{12g_m g_A}{(1 + \bar{w})^2}, \end{aligned} \quad (4.11c)$$

$$\frac{d g_A}{dl} = 8g_A^2 + 2g_m(\tilde{g}_u + g_m), \quad (4.11d)$$

$$\begin{aligned} \frac{d g_m}{dl} &= 2g_m(g_m - \tilde{g}_u) + 4g_A \tilde{g}_u + 4 \left(\frac{1 - 3\bar{w}}{1 + \bar{w}} \right) g_m g_A \\ &\quad + 2g_m \eta \bar{w} f_3(\bar{w}). \end{aligned} \quad (4.11e)$$

As discussed below in Sec. IV E, statistical SU(2) Fermi space (κ) rotational symmetry is *generically* restored under integration of the full flow equations, Eq. (4.1); we will therefore focus upon the restricted flow equations (4.11) when we discuss our primary results in Sec. IV E.

Note that Eq. (4.11d) implies that the only non-trivial fixed point structure (a fixed line) occurs in these restricted equations when $g_A = g_m = 0$ (since the disorder parameters, being variances [Eq. (2.11)], cannot take negative values).

D. Graphene with non-generic disorder

Before analyzing graphene subject to generic (short-range correlated), time-reversal invariant disorder, we discuss several simpler limiting cases that arise upon fine-tuning the disorder distribution defined by Eqs. (2.9) and (2.11). To do so, we specialize the flow Eq. (4.1) to the quantum disorder universality classes discussed in subsections II A 1–II A 3. Although it is typically difficult to fine-tune the disorder profile experimentally, some of the limiting cases discussed below may dominate various scaling or crossover regimes in graphene. (See also Sec. V.)

1. Scalar potential disorder and the symplectic class AII

If remote charged impurities provide the principal scattering mechanism in the experiments discussed in Refs. 1–4, one would expect fluctuations in the potential $u(\mathbf{r})$ to dominate over the other disorder types. As a zeroth order approximation, we may neglect the other disorder potentials altogether, setting $g_A = g_{A3} = g_m = g_v = 0$ [Eqs. (2.9) and (2.11)]. As discussed in Sec. II A 1, this is equivalent to enforcing SU(2) valley space rotational symmetry [invariance of Eq. (2.9) under κ -space rotations] *in every realization of the static disorder*. This theory satisfies the effective TRI* condition, defined by Eq. (2.7), and belongs to the symplectic (“spin-orbit”) ordinary metal class AII.^{19–24} The flow equations are

$$\frac{d \ln \bar{w}}{dl} = \tilde{g}_u - \eta \bar{w} f_3(\bar{w}), \quad (4.12a)$$

$$\frac{d \tilde{g}_u}{dl} = \frac{2 \tilde{g}_u}{1 + \bar{w}} \left[\tilde{g}_u - \eta \bar{w} f_3(\bar{w}) \right]. \quad (4.12b)$$

These equations possess an unstable fixed line for $\tilde{g}_u = \eta \bar{w} f_3(\bar{w})$; moreover,

$$g_u(l) = C \bar{w}^2(l), \quad (4.13)$$

where $C = g_u(0)/\bar{w}^2(0)$, so that the RG flows are parabolic trajectories in the $g_u - \bar{w}$ plane. [$g_u = \tilde{g}_u(1 + \bar{w})^2$ is the unscreened scalar potential disorder strength; see Eq. (2.26).]

A similar result was found previously for the case of graphene at weak Coulomb interaction coupling;^{32,33} in the case of the large- N generalization, a technical error in Ref. 32 (see Sec. III A and Appendix A) led to the prediction that the line parameterized by Eq. (4.13) becomes attractive at larger Coulomb interaction strengths. Instead, Eq. (4.12), coupled with the monotonic behavior of $\bar{w} f_3(\bar{w})$, [Eqs. (4.4)–(4.6) and Fig. 14], shows that this line is repulsive for all $\bar{w} \geq 0$. In other words, for the case of scalar potential disorder only, the physics in both the weak coupling and large- N pictures is qualitatively the same. The stability of the \tilde{g}_u - \bar{w} fixed line in the full 6-dimensional disorder-interaction coupling constant space is analyzed in Appendix B.

2. Particle-hole symmetry and the chiral class BDI

As discussed below Eq. (2.11) in Sec. II A, different quantum disorder (random matrix) universality classes may be theoretically realized by enforcing invariance of the graphene system, in every realization of disorder, under different combinations of the transformations defined by Eqs. (2.4)–(2.7). If we enforce both particle-hole symmetry (PH) and time-reversal invariance (TRI) [Eqs. (2.4) and (2.5)] in every static disorder realization, consistent with, e.g., the presence of carbon atom vacancies (treated as scattering centers in the unitary, hard-scattering limit) and the absence of further-neighbor hopping,⁵² then the system falls into the “chiral orthogonal” class BDI.^{20,27–29,40,41} The allowed disorder strengths are g_m and g_{A3} , and the one-loop flow equations are

$$\frac{d \ln \bar{w}}{dl} = 2g_{A3} + 2g_m - \eta \bar{w} f_3(\bar{w}), \quad (4.14a)$$

$$\frac{d g_{A3}}{dl} = 2g_m^2, \quad (4.14b)$$

$$\frac{d g_m}{dl} = 2g_m \eta \bar{w} f_3(\bar{w}). \quad (4.14c)$$

These equations possess no fixed point for $g_m \neq 0$, and generically flow to both strong disorder ($g_{A3}, g_m \rightarrow \infty$) and strong interaction ($\bar{w} \rightarrow \infty$) coupling. In passing, we note that, in the absence of Coulomb interactions ($\bar{w} = 0$), Eqs. (4.14) can be extended to all orders in g_m and g_{A3} , using conformal field theory methods.²⁸ One then finds that disordered graphene with strict particle-hole symmetry [Eq. (2.4)] and no long- or short-ranged interparticle interactions³⁴ possesses a critical, delocalized phase, indicative of the existence of extended single-particle states at zero energy, for arbitrary strength disorder.

The theory with $g_m = 0$ does possess an attractive fixed line in the g_{A3} - \bar{w} plane. This line has been discussed before;^{32,33} it is unlikely to play an important role in real graphene physics, because it is highly unstable in other disorder directions, as shown in Appendix B.

3. Vector potential disorder, ripples and topological defects: class CI

If we enforce both PH* and TRI [Eqs. (2.6) and (2.5)], then the system falls into the CI quantum disorder class.^{20,40,41} Recall from Sec. II A that PH* describes an *effective* particle-hole transformation, different from the physical PH transformation defined by Eq. (2.4), the latter of which is inherited directly from the lattice model [Eq. (2.1)]. The allowed disorder strengths are g_{A3} and g_A , i.e. the pure Dirac theory perturbed only by a quenched, SU(2) non-Abelian vector potential.

As discussed in Sec. II A 2, the intravalley (Abelian) vector potential $\{A_\alpha^3\}$ appears in the description of long wavelength “ripples” in the low-energy Dirac

theory.^{5,11,12} Both the intravalley and intervalley $\{A_{\alpha}^{\bar{\beta}}\}$ vector potential components play a primary role in the field theoretic description of honeycomb lattice dislocations and disclinations.³⁶

The RG flow equations are

$$\frac{d \ln \bar{w}}{dl} = 4g_A + 2g_{A3} - \eta \bar{w} f_3(\bar{w}), \quad (4.15a)$$

$$\frac{dg_A}{dl} = 8g_A g_{A3}, \quad (4.15b)$$

$$\frac{dg_{A3}}{dl} = 8g_A^2. \quad (4.15c)$$

These equations possess no fixed point for $g_A \neq 0$, and generically flow to both strong disorder and interaction coupling. In the absence of interactions, $\bar{w} = 0$, the Dirac theory with only non-Abelian vector potential disorder flows to strong coupling; the flow terminates at an exactly-solvable conformal field theory fixed point^{18,26} [equivalent to the $\text{Sp}(2n)$ principal chiral nonlinear sigma model, augmented with a WZW term].⁴⁰ Like the non-interacting BDI class discussed above, the fixed point of the non-interacting CI class model (with both g_A and g_{A3} nonzero) describes a critical, delocalized phase possessing extended wavefunctions near zero energy.^{18,26} This disorder class (in the absence of interactions) was discussed specifically in the context of graphene in Ref. 20; these authors argued that the conductance of the non-interacting CI class model should be of order the conductance quantum, and independent of the disorder strength.

E. Graphene: generic disorder

At last, we turn to an analysis of our large- N graphene field theory, characterized by the full one-loop RG flow equations (4.1). In the absence of any fine-tuning of the disorder potentials, our graphene model possesses time-reversal invariance [Eq. (2.5)] and (physical) spin $\text{SU}(2)$ rotational symmetry in every disorder realization. This system is in the standard orthogonal metal class AI. In the absence of interactions, all single particle wavefunctions are expected to be exponentially localized in 2D.⁴⁴

The full flow Eqs. (4.1b)–(4.1g) possess several fixed line structures involving a *single* nonzero disorder parameter and the Coulomb interaction strength \bar{w} . The case of scalar potential disorder \tilde{g}_u was discussed above, in Sec. IV D 1. Weak coupling analogs of this and other fixed lines were discussed in Refs. 32,33, while large- N versions were obtained and analyzed in Ref. 32 [but see the discussion following Eq. (4.13), above]. We will not dwell upon these structures here, however, because all of them are exceedingly unstable in the full 6-dimensional disorder-interaction coupling constant space. (This fact is demonstrated explicitly in Appendix B.)

The RG flow equations [Eq. (4.1)] possess no perturbatively accessible, isolated fixed points, other than

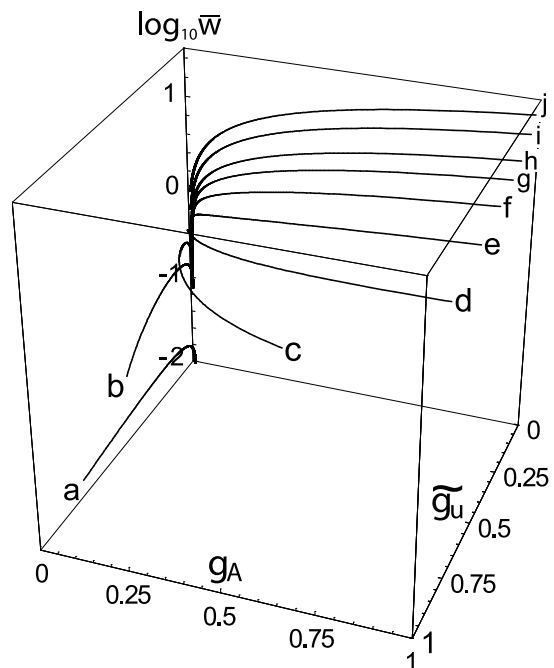


FIG. 15: Set of 10 RG flow trajectories obtained via numerical integration for different initial Coulomb interaction strengths \bar{w} . Here, we study the case with $\text{SU}(2)$ valley space symmetry restored *on average*, using Eq. (4.11). The initial conditions for the disorder coupling strengths are $\tilde{g}_u(0) = g_A(0) = g_m(0) = 0.01$ for all trajectories shown in the figure. We have set the expansion parameter $\eta = 0.3$ [see Eq. (4.3)]; the shape of the trajectories is only weakly dependent upon η (within our one-loop approximation). Lower-case Latin letters label trajectories with different initial Coulomb interaction strengths, given by $\bar{w} =$ (a) 0.010, (b) 0.079, (c) 0.13, (d) 0.16, (e) 0.20, (f) 0.25, (g) 0.32, (h) 0.40, (i) 0.63 (j) 1.0. We do not exhibit the RG evolution of the random mass parameter g_m [see Eqs. (2.9), (2.11), (4.11)], because we find that its behavior is always subleading compared to the scalar (\tilde{g}_u) or vector (g_A) potential parameters.

the (trivial) non-interacting, clean (not disordered) Dirac fixed point, defined by the condition

$$\bar{w} = \tilde{g}_u = g_A = g_{A3} = g_m = g_v = 0. \quad (4.16)$$

In order to glean information about graphene's low-energy physics (to order $1/N$ in our large- N calculational scheme), it is necessary to integrate the flow equations, and observe the evolution of the flow trajectories as a function of initial conditions in coupling constant space. In doing so, we seek to address two crucial questions that so far remain unanswered:

1. Over what range of initial conditions, if any, does the theory flow back to the clean, non-interacting Dirac fixed point [Eq. (4.16)]. In other words, can we find a critical manifold of codimension 0, with the Dirac fixed point as its sink?
2. If the clean, non-interacting Dirac fixed point is found to be unstable, where does the system flow

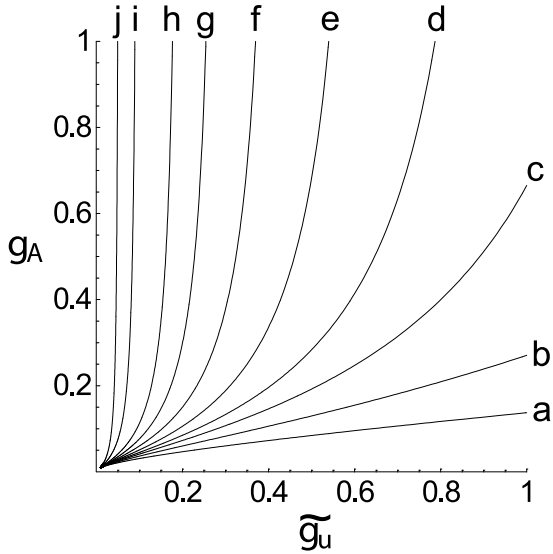


FIG. 16: Same RG trajectories shown in Fig. 15, but projected into the $\tilde{g}_u - g_A$ disorder plane.

to? What is the correct low-energy theory that we should use to understand disordered, interacting graphene?

We can easily answer the first question, but we will be forced to speculate regarding the second.

We have numerically integrated Eqs. (4.1b)–(4.1g) over a wide range of disorder and interaction coupling strength initial conditions. In our one-loop approximation, the resulting flow topology is only weakly dependent upon the expansion parameter η , defined by Eq. (4.3). We find that the non-disordered, non-interacting Dirac fixed point, located by Eq. (4.16), as well as the *entirety* of the adjoining clean, but Coulomb-interacting line, $0 \leq \bar{w} < \infty$ and $\tilde{g}_u = g_A = g_{A3} = g_m = g_v = 0$, is unstable in the presence of arbitrarily weak, but generic disorder [i.e. all five disorder strength parameters in Eq. (4.1) nonzero, but arbitrarily small]. We stress that the entirety of the clean, interacting line $\bar{w} \geq 0$ is perturbatively accessible in the $N \rightarrow \infty$ limit, and flows back to the non-interacting Dirac fixed point in the *absence* of disorder.^{31,35}

In the advent of nonzero quenched randomness, the flow to strong coupling exhibits two key features: a) SU(2) valley space rotational symmetry is generically restored *on average* upon integration of Eq. (4.1) for general initial conditions, i.e. the differences $(|g_A - g_{A3}|)/(g_A + g_{A3})$ and $(|g_m - g_v|)/(g_m + g_v)$ asymptote to zero as the solutions to the RG equations reach the limit of their validity. From here on in, we will therefore restrict our discussion to the flows of the valley space SU(2)-symmetric system, described by Eq. (4.11). b) The *direction* of the diverging RG flows depends strongly upon the initial strength of the Coulomb interaction parameter \bar{w} . For weak (or vanishing) Coulomb interactions $\bar{w} \ll 1$, the flow is dominated by the divergence of the

screened scalar potential disorder parameter \tilde{g}_u [defined by Eq. (2.26)]. The ratio of the other disorder strengths g_A and g_m to \tilde{g}_u asymptotes toward zero as the flow begins to diverge. For stronger values of the Coulomb interaction strength $\bar{w} \gtrsim 0.1$ (for the choice $\eta = 0.3$), we observe a “crossover” in the flow direction. In the limit of large Coulomb strength $\bar{w} \gtrsim 1$, we find that the flow becomes dominated by the divergence of the SU(2) non-Abelian vector potential disorder parameter g_A ; in this regime, the ratio of the other disorder strengths \tilde{g}_u and g_m to g_A asymptotes to zero as the flows leave the perturbatively accessible regime.

We demonstrate the picture described above with a selection of RG flow trajectory plots. Figs. 15–18 depict two sets of flow trajectories obtained via numerical integration of Eqs. (4.11b)–(4.11e) for different initial Coulomb interaction strengths \bar{w} . Figs. 15 and 17 depict projections of these flows in the 3D coupling constant subspace $(\tilde{g}_u, g_A, \bar{w})$. Figs. 16 and 18 respectively exhibit 2D projections of the same flows represented in Figs. 15 and 17 in the disorder plane (\tilde{g}_u, g_A) . We choose *not* to exhibit the RG evolution of the random mass parameter g_m [Eqs. (2.9), (2.11), and (4.11e)] in these figures, because we find that g_m always plays a subleading role relative to either the scalar \tilde{g}_u or non-Abelian vector g_A potential disorder strengths.

In each of Figs. 15–18, all trajectories share a given set of initial disorder strengths (described in the figure cap-

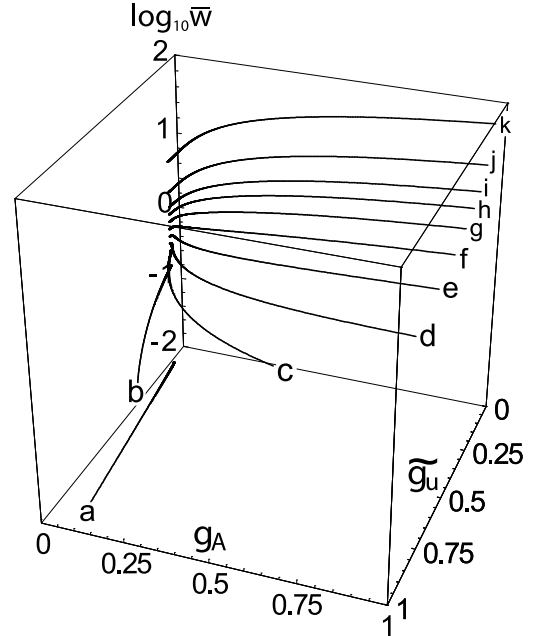


FIG. 17: As in Fig. 15 but with the initial conditions for the disorder coupling strengths $\tilde{g}_u(0) = g_m(0) = 0.1$, $g_A = 0.01$. Lower-case Latin letters label trajectories with different initial Coulomb interaction strengths, given by $\bar{w} =$ (a) 0.010, (b) 0.25, (c) 0.40, (d) 0.50, (e) 0.63, (f) 0.79, (g) 1.0, (h) 1.3, (i) 1.6, (j) 2.5, (k) 6.3.

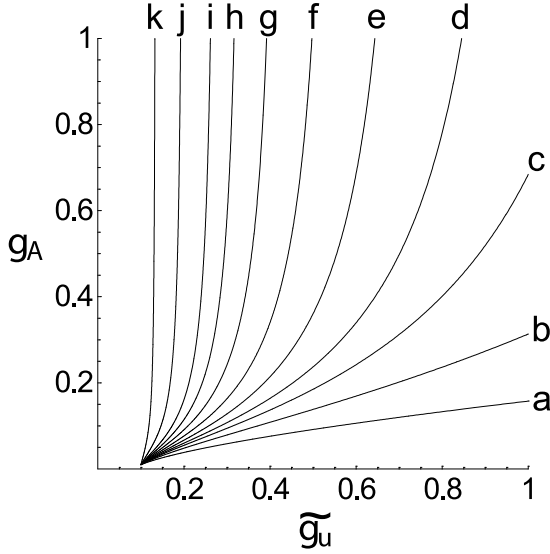


FIG. 18: Same RG trajectories shown in Fig. 17, but projected into the $\tilde{g}_u - g_A$ disorder plane.

tions). Different trajectories, distinguished by lowercase Latin letters, correspond to different initial Coulomb interaction strengths $\bar{w}(0)$. Trajectories with successive labels (a), (b), etc. carry successively larger initial values of \bar{w} ; numerical values are stated in the captions of Figs. 15 and 17. Although very weak initial Coulomb interaction strengths $\bar{w} \lesssim 0.1$ lead to trajectories that are dominated by large scalar potential disorder fluctuations $\tilde{g}_u \rightarrow \infty$, stronger initial interaction strengths bend the trajectories away from the $\tilde{g}_u - \bar{w}$ plane, toward the particle-hole symmetric $g_A - \bar{w}$ plane. [The *effective* particle-hole symmetry is defined by the PH* transformation given by Eq. (2.6)].

These figures encapsulate our primary result: non-Abelian vector potential disorder dominates the flow toward strong coupling ($g_A, \bar{w} \rightarrow \infty$) for moderate to strong Coulomb interaction strengths. As stated above, this result is essentially independent of our expansion parameter η , defined by Eq. (4.3), for our one-loop flow equations (4.1) and (4.11), obtained to lowest nontrivial order in $1/N$ and in the disorder strengths \tilde{g}_u, g_A, g_m . Physically, strong scalar potential disorder fluctuations would favor the accumulation of electrons and holes in spatially segregated “puddles,” locally violating charge neutrality. The advent of a second type of disorder that manifestly preserves a type of particle-hole symmetry [Eq. (2.6)] allows the system to flow toward a strongly disordered, interacting regime, while everywhere preserving electroneutrality. Equivalently, Coulomb interparticle interactions lead to screening effects, which parametrically curtail the scalar potential disorder fluctuations; the non-Abelian vector potential is not affected by the interactions because it represents charge-neutral randomness (such as the vector potential component of “ripples”).

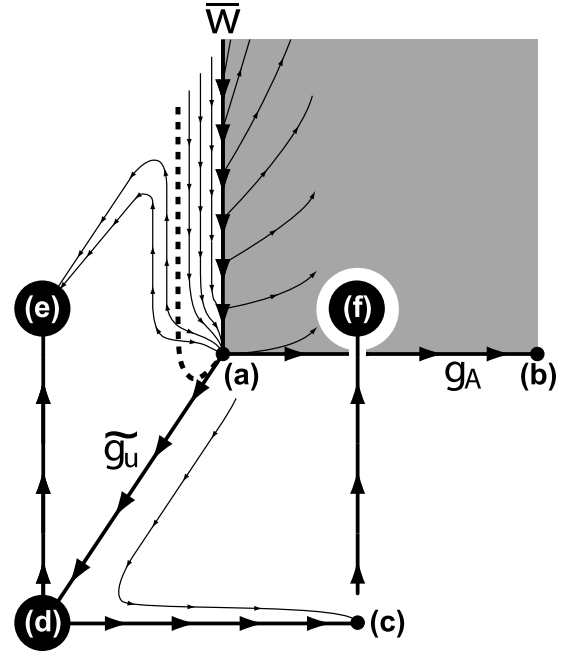


FIG. 19: Schematic phase diagram for disordered, interacting graphene, projected into the disorder (\tilde{g}_u, g_A) interaction (\bar{w}) coupling constant space, based in part upon the perturbative RG calculations performed at weak coupling,^{19,33} and within the large- N approximation (as detailed in this paper). The labeled small dots represent “known” phases, while the large black globes represent “non-linear sigma model (NL σ M) arenas,” wherein the system is described by a well-known (if poorly understood) model, which may possess multiple phases in $d = 2$ spatial dimensions.^{44,51} Point (a) represents non-interacting, clean (not disordered) graphene, as located by Eq. (4.16). This theory is a sink for the clean, Coulomb interacting line (the vertical axis), as well as a portion of the $\tilde{g}_u - \bar{w}$ plane. It is unstable to generic disorder perturbations. The dashed line in the $\tilde{g}_u - \bar{w}$ is the unstable fixed line located by Eqs. (4.12a) and (4.12b). The point (b) is the non-interacting, non-Abelian SU(2) vector potential disorder CFT.^{18,26} Both points (a) and (b) are embedded in the particle-hole symmetric plane $\tilde{g}_u = g_m = 0$, represented by the shaded plane in the figure. Point (c) represents the non-interacting Anderson insulator for the orthogonal metal class (AI) in 2D. Globe (d) should be described by the symplectic/spin-orbit class (AII), non-interacting NL σ M, possibly augmented by a topological term.^{19–24} In principle, both diffusive metallic and Anderson insulating phases are possible.⁴⁴ Globe (e) represents the symplectic class Finkel’stein non-linear sigma model (FNL σ M) for interacting electrons;^{51,53,54} globe (f) represents the orthogonal class (AI) FNL σ M.^{51,55,56} The numerical RG flows exhibited in Figs. 15 and 17 should be “superimposed” upon this figure.

To close this section, we direct the reader’s attention to Fig. 19. In this figure, we exhibit a putative phase diagram for graphene, projected into the 3D ($\tilde{g}_u, g_A, \bar{w}$) disorder-interaction coupling strength space, based upon our work here, as well as previous results^{18,20,51,55,56} regarding the zero temperature ground state physics of 2D disordered and/or interacting electronic systems. The

most important features of this figure are the points labeled (a)–(c) and the “globes” labeled (d)–(f). Points (a)–(c) label known phases of the graphene model in the *absence* of interactions: (a) is the non-disordered, non-interacting Dirac theory. (b) denotes the critical, delocalized phase that occurs at strong non-Abelian vector potential (“chiral”) disorder, described analytically by the class CI conformal field theory.^{18,26} As discussed in Secs. II A 2 and IV D 3, the class CI fixed point is expected to possess a non-zero conductance at zero temperature that is independent of the disorder strength.²⁰ Finally, (c) denotes the Anderson insulating phase for the orthogonal normal metal quantum disorder class. Globe (d) represents a “theory arena” corresponding to the symplectic (spin-orbit) normal metal class for non-interacting electrons, described by the symplectic nonlinear sigma model (possibly modified by a topological term).^{21–24} The symplectic class may possess both metallic and insulating states in 2D.⁴⁴

Globes (e) and (f) respectively describe the symplectic and orthogonal normal metal quantum disorder classes, augmented with long-range Coulomb interparticle interactions.^{51,53–56} These globes describe physics on temperature scales less than the elastic scattering rate, i.e. $T \lesssim 1/\tau_{el}$, with τ_{el} the elastic scattering lifetime due to impurity scattering. The low-energy field theory description takes the form of a modified nonlinear sigma model that incorporates electron-electron interactions.^{51,55} The Drude conductivity computed in the regime $T \sim \tau_{el}$, discussed in the next section, enters through the bare diffusion constant of the sigma model.

Arrows in Fig. 19 schematically denote RG flows whose topology has either been derived in this paper, previous work,⁵¹ or may be inferred by general principles. The dashed line residing in the \tilde{g}_u – \bar{w} plane represents the repulsive fixed line described in Sec. IV D 1; the section of the \tilde{g}_u – \bar{w} plane between this line and the Coulomb interaction (\bar{w}) axis drains into the clean, non-interacting Dirac fixed point (a). This section is, however, highly unstable in the other disorder (i.e. g_A) directions. The reader should imagine “superimposing” the flow trajectories depicted in Figs. 15 and 17 upon this figure.

V. PHYSICAL RESULTS AND DISCUSSION

In this section, we articulate a number of predictions for the scaling behavior of the dc electrical conductivity, as well as the thermal transport, for graphene in its Drude/Boltzmann transport regime. The predictions are extracted from the large- N , weak disorder renormalization group (RG) analysis performed above. We presuppose here that the temperature is sufficiently high so that quantum interference corrections to the conductivity due to electronic diffusion (weak localization and Altshuler-Aronov-type interaction effects) may be ignored.^{44,57,58}

We restore Planck’s constant via $\hbar = 2\pi$ throughout this section.

A. Disorder vs. interaction limited transport coefficients

The kinetic transport coefficients in graphene are explicit functions of the effective disorder and interaction strengths, depending upon both the elastic transport lifetime τ_{el} due to impurity scattering, and upon the inelastic transport lifetime τ_{in} due to electron-electron collisions. Estimates for these are

$$\frac{\hbar}{\tau_{el}} \propto \tilde{\mathcal{G}}_T \max(|\mu|, T), \quad (5.1a)$$

$$\frac{\hbar}{\tau_{in}} \propto \frac{1}{N} \min(\bar{w}^2, 1) \min(T, \frac{T^2}{|\mu|}), \quad (5.1b)$$

where μ is the chemical potential, T is the temperature, and $\tilde{\mathcal{G}}_T$ is a certain combination of the disorder parameters in Eq. (2.11)—see Eqs. (5.3) and (5.4), below. [Recall that $\bar{w} \propto r_s$, Eq. (2.24).]

We consider the two limits with large and small τ_{el}/τ_{in} in turn:

1. $\tau_{el} > \tau_{in}$: interaction-limited

Real, inelastic electron-electron collisions play an important role in determining the kinetic coefficients for $\tau_{el} > \tau_{in}$. In particular, at exactly zero doping $\mu = 0$, the composite electron-hole fluid is electrically neutral. Here, electron-hole collisions are enough to set a finite dc conductivity σ_{dc} , which takes the form

$$\sigma_{dc} \propto \frac{N^2 e^2}{h} \frac{1}{\min(\bar{w}^2, 1)}. \quad (5.2)$$

For Coulomb interaction strengths $\bar{w} \gtrsim 1$, Eq. (5.2) predicts a “minimum metallic conductivity” that is independent of both the interaction and disorder strengths (to a first approximation). The doping dependence of the conductivity is limited by the impurity scattering.

Violations of Mott’s formula [Eq. (5.6)] for the thermopower and of the Wiedemann-Franz law for the thermal conductivity are expected in the interaction-limited regime. Quantitative results based on the relativistic hydrodynamics description of the electron-hole plasma in graphene will appear elsewhere.⁵⁹

2. $\tau_{el} < \tau_{in}$: disorder-limited

When τ_{in} due to electron-electron collisions exceeds τ_{el} due to the impurities, the situation is simpler. To the first approximation, we can neglect contributions to the kinetic coefficients due to inelastic processes. The Drude conductivity in the ladder approximation then takes the form

$$\sigma_{dc} = \frac{N e^2}{h} E_F \tau_{el}, \quad (5.3)$$

where⁵⁹

$$E_F \tau_{el} = \frac{1}{\pi \tilde{\mathcal{G}}_T}, \quad (5.4a)$$

$$\tilde{\mathcal{G}}_T \equiv \tilde{g}_u + 8g_A + 4g_{A3} + 6g_m + 3g_v. \quad (5.4b)$$

Note that it is the *screened* scalar potential disorder parameter \tilde{g}_u [Eq. (2.26)] that appears in Eq. (5.4). The temperature or chemical potential-dependence of the conductivity follows from combining the scaling predictions of Sec. IV with Eq. (5.3); Mott’s formula and Wiedemann-Franz apply for thermotransport. In the remainder of this section, we will use this strategy to identify three scaling regimes for the transport coefficients in the disorder-limited case.

B. Scaling predictions for graphene transport

The essential message is as follows: if the disorder distribution is sufficiently weak and short-range correlated, then the RG generically predicts corrections to the conductivity that are logarithmic in temperature. In particular, we have identified three scaling regimes which may be observed in (future) graphene experiments: (1) a “QED” regime, wherein the conductivity *increases* with decreasing temperature, as well as (2) intermediate and (3) “QCD” regimes, characterized by a conductivity that decreases monotonically with decreasing temperature. Here, the descriptors “QED” and “QCD” refer to formal analogies between the disordered, interacting graphene theory in particular scaling regimes, and the theories of high energy quantum electro- and chromodynamics, respectively; we do *not* imply a mapping between experimental phenomena in high energy particle and graphene physics.

In this subsection, we set $N = 4$, appropriate to real graphene. To spare the reader from technical details, the derivation of the formulae presented below has been relegated to Appendix C. A sketch of our results is pictured in Fig. 20.

1. “QED” regime: Scalar potential disorder and flow toward weak coupling

The bare Coulomb interaction strength $r_s = e^2/\epsilon\hbar v_F$ is of order unity in the previous substrate-supported experiments,^{1–4} and should exceed two for suspended films.¹¹ As discussed in Secs. I and IV, an $r_s \sim 1$ represents a relatively strong coupling regime for the massless Dirac electrons in undoped graphene. If the disorder effects are weak relative to the Coulomb interaction strength, then the RG predicts the existence of a “QED” scaling regime, wherein disorder and electron correlation effects grow ever *weaker* on larger length or lower energy scales. This scaling toward weak coupling manifests itself as a logarithmic-squared increase in the dc conductivity with decreasing temperature [Eq. (5.5), below]. A

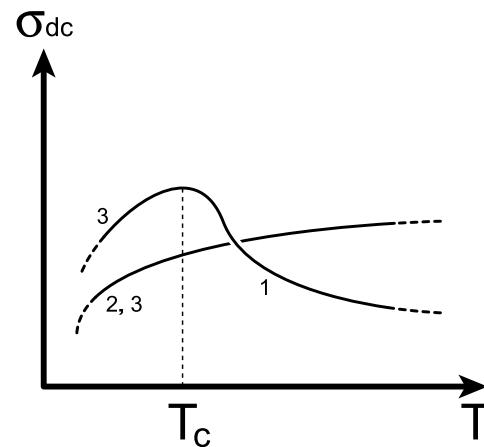


FIG. 20: Sketch of possible logarithmic scaling regimes of the dc conductivity σ_{dc} vs. temperature in undoped graphene. The labels (1)–(3) identify the qualitative scaling behaviors pictured here with the three regimes respectively discussed in subsections VB 1–VB 3 in the text. Non-monotonic behavior, i.e. the peak separating the curve segments labeled (1) and (3) in the figure, can occur if a sample microscopically dominated by strong Coulomb interactions and weak scalar potential disorder (“QED” regime), distinguished by a conductivity that increases with decreasing temperature [Eq. (5.5)], crosses over at lower temperatures to the strong coupling (“QCD”) regime dominated by non-Abelian vector potential disorder, characterized by a decreasing conductivity [Eq. (5.10)]. An intermediate scaling regime (2) is also possible, characterized by a monotonically decreasing conductivity [Eq. (5.8)]. These predictions require that $\tau_{el} < \tau_{in}$; see text.

further requirement to reach the “QED” scaling regime is that scalar potential disorder must provide the dominant scattering mechanism for the Dirac electrons. (Consult Secs. II A 1–II A 3, IV D 1, and the last paragraph of Sec. IV E.)

In this “QED” regime, we find that (see Appendix C for details)

$$\sigma_{dc}(T) \sim \frac{4e^2}{h\pi} \frac{r_s^2}{16\tilde{g}_u} \ln^2 \left(\frac{T_R}{T} \right), \quad (5.5)$$

where $T_R \gg T$ is an arbitrary reference temperature, and $\tilde{g}_u \ll r_s \sim 1$ is the microscopic strength of the (screened) scalar potential disorder [Eqs. (2.9)–(2.11), (2.26)].

The behavior described by Eq. (5.5) cannot persist indefinitely, because the presence of other disorder parameters will eventually induce a crossover to the “QCD” regime described below in subsection VB 3. This crossover would be distinguished by a *non-monotonicity* of the conductivity, as shown in Fig. 20. We do not provide here an estimate for the non-universal crossover temperature T_c , which is difficult to extract quantitatively because it depends upon the details of the full microscopic disorder distribution.⁶⁰

We also discuss thermotransport. We neglect interaction contributions or corrections to the energy current of the Dirac electrons; as a result, we find that the thermal

conductivity is slaved to Eq. (5.5) via the Wiedemann-Franz law. Within this same approximation, the thermopower S is given by Mott's formula⁶¹ ($k_B = 1$):

$$S \sim -\frac{\pi^2 T}{3 e} \frac{d \ln \sigma_{\text{dc}}(\epsilon)}{d\epsilon}. \quad (5.6)$$

In this expression, $\sigma_{\text{dc}}(\epsilon)$ is the scaling form of the conductivity, with temperature replaced by ϵ (i.e. the chemical potential). Using Eq. (5.5), we obtain

$$S \sim \frac{\pi^2 T}{3 e} \frac{2}{\mu \ln(\mu_R/\mu)}, \quad (5.7)$$

for $|\mu| > T$, with $\mu_R > \mu$.

2. *Intermediate regime: Scalar potential disorder and flow toward strong coupling*

We next consider the case where the strength of the Coulomb interaction r_s is made weaker than that of the screened scalar potential disorder fluctuations [$\tilde{g}_u \gtrsim \bar{w} \sim r_s$]. We also require that scalar potential fluctuations provide the dominant source of scattering for the Dirac electrons, while not becoming so strong so as to invalidate our weak disorder assumption ($\tilde{g}_u \lesssim 1$). Such a scenario might prove difficult to realize experimentally, but could be achieved in principle by screening the long-ranged Coulomb interactions with an external gate (brought into very close proximity to the graphene layer), or by coating graphene with a high- k dielectric material.

The scaling behavior of the conductivity in this regime is given by

$$\sigma_{\text{dc}}(T) \sim \frac{4e^2}{h\pi} \left[\frac{1}{\tilde{g}_u} - 2 \ln \left(\frac{T_R}{T} \right) \right], \quad (5.8)$$

for $T_R > T$ (Appendix C).

The thermopower at non-zero chemical potential $|\mu| > T$ is given by

$$S \sim -\frac{\pi^2 T}{3 e} \frac{2\tilde{g}_u}{\mu}. \quad (5.9)$$

3. *“QCD” regime: Non-Abelian vector potential disorder and asymptotic flow toward strong coupling*

Non-abelian vector potential disorder provides another potentially important scattering mechanism in graphene.^{5,11,12} This disorder type arises in the context of elastic deformations or “ripples” and in the context of topological lattice defects.³⁶ (See also Secs. II A 2 and IVD 3.)

Surprisingly, we have found in this paper that quenched vector potential disorder generically emerges as the dominant scattering mechanism at long length scales and low energies for Dirac electrons with a bare

Coulomb interaction parameter $r_s \gtrsim 0.1$. [See Sec. IV E for details.] In this regime, the graphene theory becomes formally analogous to 3+1-D quantum chromodynamics (QCD), in that the system becomes dominated by strong non-Abelian vector potential disorder and electron correlation effects (due to the Coulomb interactions). The essential difference between graphene and real QCD is that in the former (latter) case, it is a static, time-independent (dynamic, gluon-mediated) non-Abelian gauge potential that drives the system toward strong coupling at low energies.

Since $r_s \gtrsim 1$ in real graphene, we generically expect to reach the “QCD” regime at some finite temperature scale. We obtain the following formula for the asymptotic scaling behavior of the conductivity (Appendix C):

$$\sigma_{\text{dc}}(T) \sim \frac{4e^2}{h\pi} \left[\frac{1}{12g_A} - \frac{2\pi^2}{3(\pi^2 - 2)} \ln \left(\frac{T_R}{T} \right) \right], \quad (5.10)$$

where g_A is the (renormalized) strength of the non-Abelian vector potential disorder, and $T_R > T$. Eq. (5.10) is not expected to hold down to arbitrarily low temperatures. As we examine lower and lower energy scales, the effective vector potential disorder strength $g_A(T)$ grows ever larger (Sec. IV E); as a result, the scaling behavior of Eq. (5.10) will mutate as g_A evolves. [A more general scaling formula in the “QCD” regime is given by Eq. (C3) in Appendix C, which reduces to Eq. (5.10) in the limit $g_A \ll 1$.]

The thermopower at finite chemical potential $|\mu| > T$ corresponding to Eq. (5.10) is given by

$$S \sim -\frac{\pi^2 T}{3 e} \frac{8g_A}{\mu} \frac{\pi^2}{\pi^2 - 2}. \quad (5.11)$$

Finally, we reiterate the following point: we have assumed that the inelastic transport lifetime due to electron-electron collisions, τ_{in} , exceeds the elastic lifetime τ_{el} due to the disorder. In graphene, the kinetic coefficients are sensitive to the value of τ_{in}/τ_{el} ; we will discuss the implications of the above three scaling regimes in the limit $\tau_{in}/\tau_{el} > 1$ in a subsequent publication.⁵⁹

Acknowledgments

We would like to thank Andreas Ludwig for helpful discussions at the beginning of this work. One of us (MSF) was supported primarily by the Nanoscale Science and Engineering Initiative of the National Science Foundation under NSF Award Number CHE-06-41523, and by the New York State Office of Science, Technology, and Academic Research (NYSTAR).

APPENDIX A: COMPUTATION OF THE ELECTRONIC SELF-ENERGY TO $O(\frac{1}{N})$.

In this appendix, we derive the amplitude given by Eq. (3.1) for the diagram $D_{5,1}$, pictured in Fig. 5. $D_{5,1}$ is

the contribution to the electronic self-energy due to the Coulomb interactions at order $1/N$. Using the Feynman rules from Sec. II B, one has

$$\mathbb{D}_{5.1} = \left(i\sqrt{\frac{w}{N}} \right)^2 \int \frac{d\omega d^2\mathbf{l}}{(2\pi)^3} \frac{i(\omega_n + \omega) + v_F \hat{\boldsymbol{\sigma}} \cdot (\mathbf{k} + \mathbf{l})}{(\omega_n + \omega)^2 + v_F^2 (\mathbf{k} + \mathbf{l})^2} \times \frac{1}{|\mathbf{l}|} \frac{\sqrt{v_F^2 l^2 + \omega^2}}{\sqrt{v_F^2 l^2 + \omega^2} + \bar{w} v_F |\mathbf{l}|}. \quad (\text{A1})$$

Expanding in terms of the external frequency and momentum, we obtain

$$\mathbb{D}_{5.1} \sim \frac{-w}{v_F N} [i\omega_n I_1 + v_F \hat{\boldsymbol{\sigma}} \cdot \mathbf{k} I_2], \quad (\text{A2})$$

where

$$I_1 = \int \frac{d\omega d^2\mathbf{l}}{(2\pi)^3} \frac{1}{|\mathbf{l}|} \frac{\sqrt{l^2 + \omega^2}}{\sqrt{l^2 + \omega^2} + \bar{w} |\mathbf{l}|} \frac{\mathbf{l}^2 - \omega^2}{(\omega^2 + \mathbf{l}^2)^2}, \quad (\text{A3a})$$

$$I_2 = \int \frac{d\omega d^2\mathbf{l}}{(2\pi)^3} \frac{1}{|\mathbf{l}|} \frac{\sqrt{l^2 + \omega^2}}{\sqrt{l^2 + \omega^2} + \bar{w} |\mathbf{l}|} \frac{\omega^2}{(\omega^2 + \mathbf{l}^2)^2}, \quad (\text{A3b})$$

and where it is useful to define

$$I_3 \equiv I_1 + I_2 = \int \frac{d\omega d^2\mathbf{l}}{(2\pi)^3} \frac{1}{|\mathbf{l}|} \frac{\sqrt{l^2 + \omega^2}}{\sqrt{l^2 + \omega^2} + \bar{w} |\mathbf{l}|} \frac{\mathbf{l}^2}{(\omega^2 + \mathbf{l}^2)^2}. \quad (\text{A3c})$$

After rescaling $\omega \rightarrow \omega |\mathbf{l}|$, the momentum integrals are trivially done, so that

$$I_2 = \frac{\ln \Lambda}{2\pi^2} \int_0^\infty dx \frac{\sqrt{1+x^2}}{\sqrt{1+x^2} + \bar{w}} \frac{x^2}{(x^2+1)^2} \quad (\text{A4a})$$

$$I_3 = \frac{\ln \Lambda}{2\pi^2} \int_0^\infty dx \frac{\sqrt{1+x^2}}{\sqrt{1+x^2} + \bar{w}} \frac{1}{(x^2+1)^2} \quad (\text{A4b})$$

where we neglect ultraviolet-finite terms associated with the infrared region of the momentum integration. We then find that

$$I_1 \equiv \frac{\ln \Lambda}{2\pi} f_1(\bar{w}), \quad (\text{A5a})$$

$$I_2 \equiv \frac{\ln \Lambda}{2\pi} f_2(\bar{w}), \quad (\text{A5b})$$

$$I_3 \equiv \frac{\ln \Lambda}{2\pi} f_3(\bar{w}), \quad (\text{A5c})$$

where the functions f_1 – f_3 were defined by Eqs. (3.3) and (3.4). Using Eq. (A5) in Eq. (A2), we recover Eq. (3.1).

APPENDIX B: FIXED LINES AND LINEARIZED FLOW EQUATIONS

The one-loop, large- N flow equations given by Eq. (4.1) in Sec. IV possess a number of critical fixed line

structures, continuously connected to the non-disordered, non-interacting Dirac fixed point [Eq. (4.16)]. In this appendix, we enumerate these structures, and determine their stability in the six-dimensional coupling strength space [c.f. Eq. (4.1)]. Each fixed line resides in a plane formed between the Coulomb interaction axis \bar{w} and a single, nonzero disorder parameter.

a. Scalar potential disorder

As discussed in Sec. IV D 1, in the case of pure scalar potential disorder, i.e. only $\tilde{g}_u > 0$ among the five disorder parameters appearing in Eq. (4.1), the large- N graphene model exhibits a repulsive fixed line in the \tilde{g}_u – \bar{w} plane. From Eq. (4.12), the fixed line is parameterized by the conditions

$$g_A = g_{A3} = g_m = g_v = 0, \quad (\text{B1a})$$

$$\tilde{g}_u^{(0)} = \eta \bar{w}^{(0)} f_3(\bar{w}^{(0)}). \quad (\text{B1b})$$

Since \tilde{g}_u and $\eta = 8/\pi N$ are expansion parameters for our large- N theory, the *entirety* of the fixed line described by Eq. (B1) is perturbatively accessible, because the function $\bar{w} f_3(\bar{w})$ asymptotes to a finite constant as $\bar{w} \rightarrow \infty$; see Eq. (4.6) and Fig. 14.

Linearizing Eq. (4.1) about the line in Eq. (B1), we obtain the following RG eigenvalues (as a function of $\bar{w}^{(0)}$):

$$\left\{ 0, \eta \bar{w}^{(0)} \left[\frac{2f_3(\bar{w}^{(0)})}{1 + \bar{w}^{(0)}} - \mathcal{F}_3(\bar{w}^{(0)}) \right], -2\sqrt{2} \eta \bar{w}^{(0)} f_3(\bar{w}^{(0)}), 2\sqrt{2} \eta \bar{w}^{(0)} f_3(\bar{w}^{(0)}) \right\}, \quad (\text{B2})$$

where we have introduced the function

$$\mathcal{F}_3(\bar{w}) \equiv \frac{d}{d\bar{w}} [\bar{w} f_3(\bar{w})] = \frac{1}{2\bar{w}^2} \left(\frac{2}{\pi} \frac{1}{1 - \bar{w}^2} \times \left[-\bar{w} + \frac{2\bar{w}^2 - 1}{\sqrt{1 - \bar{w}^2}} \arccos(\bar{w}) \right] + 1 \right). \quad (\text{B3})$$

The first two eigenvalues listed in Eq. (B2) respectively characterize RG flow trajectories along and through the fixed line within the \tilde{g}_u – \bar{w} plane; the latter two eigenvalues listed in this equation characterize the RG flow in the transverse directions, and are each doubly degenerate. The second and fourth eigenvalues listed in Eq. (B2) are positive for all finite $\bar{w}^{(0)} > 0$; both the $\tilde{g}_u^{(0)}(\bar{w}^{(0)})$ fixed line, as well as the portion of the \tilde{g}_u – \bar{w} plane spanning the region between this fixed line and the \bar{w} -axis are therefore highly unstable.

b. *Abelian vector potential disorder*

Next, we consider the following fixed line in the $g_{A3}-\bar{w}$ plane:

$$\tilde{g}_u = g_A = g_m = g_v = 0, \quad (\text{B4a})$$

$$g_{A3}^{(0)} = \frac{\eta}{2} \bar{w}^{(0)} f_3(\bar{w}^{(0)}). \quad (\text{B4b})$$

Linearizing Eq. (4.1) along this line, we obtain the eigenvalues

$$\left\{ 0, -\eta \bar{w}^{(0)} \mathcal{F}_3(\bar{w}^{(0)}), 2\eta \bar{w}^{(0)} f_3(\bar{w}^{(0)}), 4\eta \bar{w}^{(0)} f_3(\bar{w}^{(0)}), \frac{2\eta \bar{w}^{(0)} f_3(\bar{w}^{(0)}) \left[1 - \bar{w}^{(0)} \pm \sqrt{2 + \bar{w}^{(0)}(\bar{w}^{(0)} - 2)} \right]}{1 + \bar{w}^{(0)}} \right\}. \quad (\text{B5})$$

The first two eigenvalues listed in Eq. (B5) respectively characterize RG flow trajectories along and through the fixed line within the $g_{A3}-\bar{w}$ plane, where it serves as a (locally) attractive, critical extension of the clean Dirac fixed point [located by Eq. (4.16)]. The latter four eigenvalues appearing in Eq. (B5) characterize the RG flow in the transverse directions, and show that this fixed line is highly unstable.

c. *Staggered potential disorder*

Finally, we consider a fixed line in the $g_v-\bar{w}$ plane, parameterized by the conditions

$$\tilde{g}_u = g_A = g_{A3} = g_m = 0, \quad (\text{B6a})$$

$$g_v^{(0)} = \eta \bar{w}^{(0)} f_3(\bar{w}^{(0)}). \quad (\text{B6b})$$

Linearizing Eq. (4.1) yields the RG eigenvalues

$$\left\{ 0, -\eta \bar{w}^{(0)} \left[2f_3(\bar{w}^{(0)}) + \mathcal{F}_3(\bar{w}^{(0)}) \right], 2(1 \pm \sqrt{3})\eta \bar{w}^{(0)} f_3(\bar{w}^{(0)}), \pm \frac{2\sqrt{2}\eta \bar{w}^{(0)} f_3(\bar{w}^{(0)})}{1 + \bar{w}^{(0)}} \right\}. \quad (\text{B7})$$

The first two eigenvalues listed in this equation respectively characterize RG flow trajectories along and through the fixed line within the $g_v-\bar{w}$ plane; the latter four characterize the RG flow in the transverse directions. We observe that the $g_v^{(0)}(\bar{w}^{(0)})$ critical fixed line is also unstable for all finite $\bar{w}^{(0)} > 0$.

APPENDIX C: DERIVATION OF PHYSICAL RESULTS

In this appendix, we derive the scaling predictions for the dc conductivity stated in Eqs. (5.5), (5.8), and (5.10) of Sec. V. These predictions arise in the ‘‘QED,’’ intermediate, and ‘‘QCD’’ scaling regimes respectively, as defined in that section.

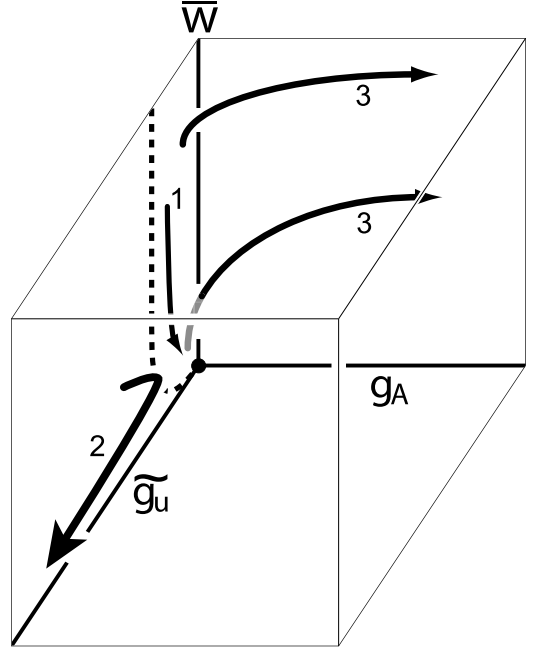


FIG. 21: Schematic RG flow diagram, projected into the 3D coupling constant space formed from the screened scalar potential disorder strength (\tilde{g}_u), the non-Abelian vector potential disorder strength (g_A), and Coulomb interaction strength ($\bar{w} = \pi r_s/2$) [Eq. (2.24)]. This diagram should be compared to the flow plots, obtained via numerical integration of Eq. (4.11), depicted in Figs. 15 and 17 of Sec. IV E. In this figure, we have sketched characteristic flows, designated by the labels (1)–(3), corresponding to the ‘‘QED,’’ intermediate, and ‘‘QCD’’ scaling regimes discussed in Sec. V. The dashed curve represents the unstable fixed line discussed below Eq. (4.12) in Sec. IV D 1.

1. ‘‘QED’’ regime: Scalar potential disorder and flow toward weak coupling

The ‘‘QED’’ regime occurs when the microscopic initial conditions are such that the (screened) scalar potential disorder fluctuations are much stronger than that of all other disorder types: $\tilde{g}_u \gg \mathcal{G}_\mu^\nu$ [see Eqs. (2.9)–(2.11), (2.26), and (2.14)]. Over some intermediate window of scaling, we would expect the RG to be dominated by \tilde{g}_u and the Coulomb interaction strength \bar{w} ; to that end, we set all other disorder parameters to zero, and integrate the RG flow described by Eq. (4.12).

As discussed in Sec. IV D 1, these flow equations possess a repulsive fixed line, pictured as the dashed curve in Figs. 19 and 21. At the end of Sec. IV E, we noted that this line divides the $\tilde{g}_u-\bar{w}$ plane into two portions; the portion joining the fixed line to the \bar{w} -axis flows back to the clean, non-interacting Dirac fixed point, while its complement flows toward strong disorder and interaction coupling. (The portion that flows back to the clean Dirac fixed point is destabilized by the other disorder parameters for arbitrarily weak but non-zero disorder strength,

as shown in Appendix B.) The RG evolves toward weak (strong) coupling at longer length and lower energy scales if the “microscopic” disorder and interaction strengths \tilde{g}_u and \bar{w} satisfy $\tilde{g}_u < \eta\bar{w}f_3(\bar{w})$ [$\tilde{g}_u > \eta\bar{w}f_3(\bar{w})$].

In the case of a flow toward weak coupling (“QED” regime), the Coulomb interaction \bar{w} rapidly decreases toward zero; we therefore take $\bar{w} \ll 1$ without loss of generality. One obtains the scaling behavior [using RG Eqs. (4.1a), (4.8), and (4.12), and Eqs. (5.3) and (5.4) for σ_{dc}]

$$\sigma_{dc}(T) \sim \frac{Ne^2}{2\pi^2} \frac{(\eta\bar{w})^2}{16g_u} \ln^2\left(\frac{T_R}{T}\right), \quad (C1)$$

where $\eta = 8/\pi N$ and $T_R \gg T$ is an arbitrary reference temperature. Setting $N = 4$, $g_u \propto \tilde{g}_u$, and replacing $\bar{w} \rightarrow \pi r_s/2$ [Eq. (2.24)], we obtain Eq. (5.5) in Sec. V.

The evolution towards weak coupling characteristic of the “QED” regime is represented via the schematic RG flow labeled (1) in Fig. 21. Although this flow approaches the clean, non-interacting Dirac fixed point [located by Eq. (4.16) in Sec. IV E], it is ultimately deflected toward the strong-coupling, “QCD” regime, labeled (3) in Fig. 21, for any non-zero, but arbitrarily small random vector potential (g_A) or random mass (g_m) disorder fluctuations.

2. Intermediate regime: Scalar potential disorder and flow toward strong coupling

We next consider the case where again $\tilde{g}_u \gg \mathcal{G}_\mu^\nu$, but now $\tilde{g}_u > \eta\bar{w}f_3(\bar{w})$, so that the RG flows toward strong coupling [Eq. (4.12)]. We further restrict $\bar{w} \ll 1$, since larger values of \bar{w} induce a crossover to the “QCD” regime dominated by the vector potential disorder, described in the next subsection.

With these assumptions, the intermediate scaling behavior of the conductivity is given by

$$\sigma_{dc}(T) \sim \frac{Ne^2}{2\pi^2} \left[\frac{1}{\tilde{g}_u} - 2 \ln\left(\frac{T_R}{T}\right) \right], \quad (C2)$$

for $T_R > T$. We recover Eq. (5.8) for $N = 4$.

The evolution of the RG in this intermediate regime is represented by the curve labeled (2) in Fig. 21.

3. “QCD” regime: Non-Abelian vector potential disorder and asymptotic flow toward strong coupling

Finally, we consider the flow toward strong coupling for moderate to strong Coulomb interactions. This is the “QCD” regime dominated by the non-Abelian vector potential disorder parameters g_A and g_{A3} . As discussed in Sec. IV E, valley space SU(2) rotational symmetry is restored on average as the RG scales toward strong coupling; we may therefore take $g_A \sim g_{A3}$.

Neglecting all disorder parameters except g_A , we integrate Eqs. (4.11a), (4.11b), and (4.11d), and combine the results with Eqs. (4.8), (5.3), and (5.4). For $\bar{w} \gtrsim 1$, we obtain the following formula for the asymptotic scaling behavior of the conductivity:

$$\sigma_{dc}(T) \sim \frac{Ne^2}{2\pi^2} \frac{1}{12g_A\phi} W \left[\phi e^\phi \left(\frac{T}{T_R} \right)^{4/3} \right], \quad (C3)$$

for $T_R > T$. In this equation,

$$\phi \equiv \frac{1}{6g_A} \left(1 - \frac{\eta}{\pi} \right), \quad (C4)$$

and $W(z)$ is Lambert’s function, i.e. solves the equation $We^W = z$. For $g_A \ll 1$, Eq. (C3) reduces to

$$\sigma_{dc}(T) \sim \frac{Ne^2}{2\pi^2} \left[\frac{1}{12g_A} - \frac{2\pi}{3(\pi - \eta)} \ln\left(\frac{T_R}{T}\right) \right], \quad (C5)$$

which is the same as Eq. (5.10) for $N = 4$ ($\eta = 2/\pi$).

The curves labeled (3) in Fig. 21 schematically indicate the flow toward strong coupling associated with the scaling prediction given by Eq. (C5) in this “QCD” regime; see also Figs. 15–18 in Sec. IV E.

* Electronic address: foster@phys.columbia.edu

¹ K. S. Novoselov, A. K. Geim, S. V. Morozov, D. Jiang, Y. Zhang, S. V. Dubonos, I. V. Grigorieva, and A. A. Firsov, *Science* **306**, 666 (2004).

² K. S. Novoselov, A. K. Geim, S. V. Morozov, D. Jiang, M. I. Katsnelson, I. V. Grigorieva, S. V. Dubonos, and A. A. Firsov, *Nature* **438**, 197 (2005).

³ Y. Zhang, Y.-W. Tan, H. L. Stormer, and P. Kim, *Nature* **438**, 201 (2005).

⁴ Y.-W. Tan, Y. Zhang, H. L. Stormer, and P. Kim, *Eur. Phys. J. Special Topics* **148**, 15 (2007).

⁵ S. V. Morozov, K. S. Novoselov, M. I. Katsnelson, F. Schedin, L. A. Ponomarenko, D. Jiang, and A. K. Geim, *Phys. Rev. Lett.* **97**, 016801 (2006).

⁶ K. Nomura and A. H. MacDonald, *Phys. Rev. Lett.* **96**, 256602 (2006).

⁷ K. Nomura and A. H. MacDonald, *Phys. Rev. Lett.* **98**, 076602 (2007).

⁸ E. H. Hwang, S. Adam, S. Das Sarma, *Phys. Rev. Lett.* **98**, 186806 (2007).

⁹ S. Adam, E. H. Hwang, V. M. Galitski, and S. Das Sarma, *Proc. Natl. Acad. Sci. USA* **104**, 18392 (2007).

¹⁰ V. V. Cheianov, V. I. Fal’ko, B. L. Altshuler, I. L. Aleiner, *Phys. Rev. Lett.* **99**, 176801 (2007).

¹¹ J. C. Meyer, A. K. Geim, M. I. Katsnelson, K. S. Novoselov, T. J. Booth, and S. Roth, *Nature* **446**, 60 (2007).

¹² A. F. Morpurgo and F. Guinea, *Phys. Rev. Lett.* **97**,

- 196804 (2006).
- ¹³ A. Fasolino, J. H. Los, and M. I. Katsnelson, *Nat. Mater.* **6**, 858 (2007).
- ¹⁴ E. Fradkin, *Phys. Rev. B* **33**, 3263 (1986).
- ¹⁵ P. A. Lee, *Phys. Rev. Lett.* **71**, 1887 (1993).
- ¹⁶ N. H. Shon and T. Ando, *J. Phys. Soc. Jpn.* **67**, 2421 (1998); H. Suzuura and T. Ando, *Phys. Rev. Lett.* **89**, 266603 (2002); Y. Zheng and T. Ando, *Phys. Rev. B* **65**, 245420 (2002); T. Ando, T. Zheng, and H. Suzuura, *J. Phys. Soc. Jpn.* **71**, 1318 (2002).
- ¹⁷ N. M. R. Peres, F. Guinea, and A. H. Castro Neto, *Phys. Rev. B* **73**, 125411 (2006).
- ¹⁸ A. A. Nersisyan, A. M. Tsvetlik, and F. Wenger, *Phys. Rev. Lett.* **72**, 2628 (1994); *Nucl. Phys. B* **438**, 561 (1995).
- ¹⁹ I. L. Aleiner and K. B. Efetov, *Phys. Rev. Lett.* **97**, 236801 (2006).
- ²⁰ P. M. Ostrovsky, I. V. Gornyi, and A. D. Mirlin, *Phys. Rev. B* **74**, 235443 (2006).
- ²¹ P. M. Ostrovsky, I. V. Gornyi, and A. D. Mirlin, *Phys. Rev. Lett.* **98**, 256801 (2007).
- ²² S. Ryu, C. Mudry, H. Obuse, and A. Furusaki, *Phys. Rev. Lett.* **99**, 116601 (2007).
- ²³ J. H. Bardarson, J. Tworzydło, P. W. Brouwer, and C. W. J. Beenakker, *Phys. Rev. Lett.* **99**, 106801 (2007).
- ²⁴ K. Nomura, M. Koshino, and S. Ryu, *Phys. Rev. Lett.* **99**, 146806 (2007).
- ²⁵ A. W. W. Ludwig, M. P. A. Fisher, R. Shankar, and G. Grinstein, *Phys. Rev. B* **50**, 7526 (1994).
- ²⁶ A. M. Tsvetlik, cond-mat/9409039; J.-S. Caux, N. Taniguchi, and A. M. Tsvetlik, *Phys. Rev. Lett.* **80**, 1276 (1998); *Nucl. Phys.* **525**, 671 (1998); A. W. W. Ludwig, cond-mat/0012189.
- ²⁷ Y. Hatsugai, X.-G. Wen, and M. Kohmoto, *Phys. Rev. B* **56**, 1061 (1997).
- ²⁸ S. Guruswamy, A. LeClair, and A. W. W. Ludwig, *Nucl. Phys. B* **583**, 475 (2000).
- ²⁹ S. Ryu and Y. Hatsugai, *Phys. Rev. B* **65**, 033301 (2002).
- ³⁰ D. Bernard, (*Perturbed*) conformal field theory applied to 2d disordered systems: an introduction, in: Cargèse lectures, NATO Science Series: Physics B, vol. 362 (1997), L. Banlieu et al. (eds.); hep-th/9509137.
- ³¹ J. Ye and S. Sachdev, *Phys. Rev. Lett.* **80**, 5409 (1998).
- ³² J. Ye, *Phys. Rev. B* **60**, 8290 (1999).
- ³³ T. Stauber, F. Guinea, and M. A. H. Vozmediano, *Phys. Rev. B* **71**, 041406(R) (2005).
- ³⁴ M. S. Foster and A. W. W. Ludwig, *Phys. Rev. B* **73**, 155104 (2006).
- ³⁵ D. T. Son, *Phys. Rev. B* **75**, 235423 (2007).
- ³⁶ J. González, F. Guinea, and M. A. H. Vozmediano, *Nucl. Phys. B* **406**, 771 (1993); P. E. Lammert and V. H. Crespi, *Phys. Rev. Lett.* **85**, 5190 (2000); J. González, F. Guinea, and M. A. H. Vozmediano, *Phys. Rev. B* **63**, 134421 (2001); M. A. H. Vozmediano, F. Guinea, M. P. López-Sancho, *J. Phys. Chem. Solids* **67**, 562 (2006).
- ³⁷ We employ the conventional basis for all Pauli matrices.
- ³⁸ Note that the TRI operation in Eq. (2.5) is appropriate only for *spinless* fermions; for spin-1/2 electrons, an additional conjugating matrix is required in spin space. Nevertheless, since we will not consider in this paper spin-dependent interparticle interactions or disorder potentials, we may adopt Eq. (2.5) as our functional definition of TRI.
- ³⁹ M. R. Zirnbauer, *J. Math. Phys.* **37**, 4986 (1996).
- ⁴⁰ A. Altland, B. D. Simons, and M. R. Zirnbauer, *Phys. Rep.* **359**, 283 (2002).
- ⁴¹ D. Bernard and A. LeClair, *J. Phys. A* **35**, 2555 (2002).
- ⁴² R. Gade and F. Wegner, *Nucl. Phys. B* **360**, 213 (1991); R. Gade, *Nucl. Phys. B* **398**, 499 (1993).
- ⁴³ The key ingredient leading to symplectic, rather than orthogonal symmetry, is the factorization of the symmetric matrix $\hat{\sigma}^2 \hat{\kappa}_2$ into antisymmetric $\hat{\sigma}^2$ and $\hat{\kappa}_2$ parts. The absence of valley-space symmetry breaking [due to the absence of disorder types in Eq. (2.9) other than $u(\mathbf{r})$] converts Eq. (2.5) into (2.7). In terms of the single-particle Hamiltonian \hat{h} , imposing Eq. (2.5) or (2.7) respectively removes an orthogonal or symplectic subalgebra from the parent unitary Lie algebra, placing \hat{h} into the orthogonal or symplectic Wigner-Dyson class, respectively.
- ⁴⁴ P. A. Lee and T. V. Ramakrishnan, *Rev. Mod. Phys.* **57**, 287 (1985).
- ⁴⁵ V. S. Dotsenko and V. S. Dotsenko, *Adv. Phys.* **32**, 129 (1983).
- ⁴⁶ T. Senthil and M. P. A. Fisher, *Phys. Rev. B* **61**, 9690 (2000).
- ⁴⁷ M. Bocquet, D. Serban, and M. R. Zirnbauer, *Nucl. Phys. B* **578**, 628 (2000).
- ⁴⁸ N. Read and A. W. W. Ludwig, *Phys. Rev. B* **63**, 024404 (2001).
- ⁴⁹ J. González, F. Guinea, and M. A. H. Vozmediano, *Phys. Rev. B* **59**, R2474 (1999).
- ⁵⁰ See e.g. D. J. Amit, *Field Theory, the Renormalization Group, and Critical Phenomena*, 2nd ed. (World Scientific, Singapore, 1984).
- ⁵¹ For a review, see e.g. D. Belitz and T. R. Kirkpatrick, *Rev. Mod. Phys.* **66**, 261 (1994).
- ⁵² See the discussion in Sec. II A 2.
- ⁵³ C. Castellani, C. DiCastro, G. Forgacs, and S. Sorella, *Solid State Commun.* **52**, 261 (1984).
- ⁵⁴ G. Kotliar and S. Sorella in *Field Theory in Condensed Matter Physics*, edited by Z. Tesaonovic (Addison Wesley, Redwood City, Calif., 1990).
- ⁵⁵ A. M. Finkel'stein, *Zh. Eksp. Teor. Fiz.* **84**, 168 (1983), *Sov. Phys. JETP* **57**, 97 (1983).
- ⁵⁶ C. Castellani et al., *Phys. Rev. B* **30**, 1596 (1984).
- ⁵⁷ I. L. Aleiner, B. L. Altshuler, and M. E. Gershenson, *Waves Random Media* **9**, 201 (1999).
- ⁵⁸ B. L. Altshuler and A. G. Aronov in *Electron-Electron Interactions in Disordered Systems*, edited by A. L. Efros and M. Pollak (North-Holland, Amsterdam, 1985).
- ⁵⁹ I. L. Aleiner and M. S. Foster, unpublished.
- ⁶⁰ The crossover between the “QED” and “QCD” regimes described in this section occurs through the RG flow equations [Eqs. (4.1) and (4.11)] in a way that involves all of the disorder parameters, not just the scalar potential g_u and non-Abelian vector potential $\{g_A, g_{A3}\}$ parameters.
- ⁶¹ See, e.g., G. D. Mahan, *Many-Particle Physics*, 3rd ed. (Kluwer Academic/Plenum Press, New York, 2000).